DESIGN AND CALCULATION OF THE VACUUM SYSTEM FOR HIGH-ENERGY LINEAR ACCELERATOR AND TEST BENCH

A01

Pilong Tian； Yongsheng Ma； Lei Zhang
Email: tianpl@ihep.ac.cn
Institute of High Energy Physics, Chinese Academies of Sciences, Beijing, China

Project one

The project involves a high-current electron linear accelerator with a maximum energy of 40 MeV. For the high-power long-pulse mode, the normal operating condition is single-pulse mode, with a beam current of 100 mA, a pulse duration of 0.1 s, and a bunch repetition frequency of 100 Hz, with a maximum average repetition rate of 10 Hz. The total length of the linear accelerator is approximately 6.3 meters, and the vacuum system is divided into four sections. Specific vacuum requirements are listed in Table 1.

Table 1: Parameters of the vacuum(unit:Pa)

Name	Static pressure[1]	Dynamic pressure[2]
Electron gun section	$<1\times10^{-7}$	$<2\times10^{-6}$
Focusing Segment	$<5\times10^{-6}$	$<1\times10^{-5}$
DUMP Section	$<5\times10^{-6}$	$<1\times10^{-5}$
Quick-adjust tube	$<5\times10^{-6}$	$<1\times10^{-5}$

Explanation:

1. Represents the pressure value when there is no microwave power or high voltage;
2. 2. Represents the pressure value under normal operating conditions.

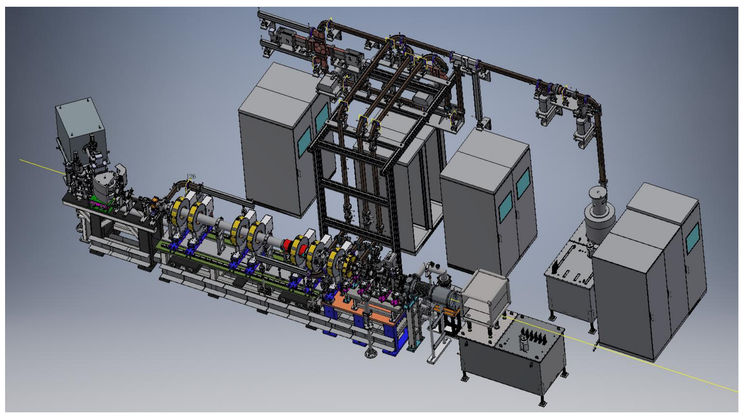

Fig. 1: Assembly drawing

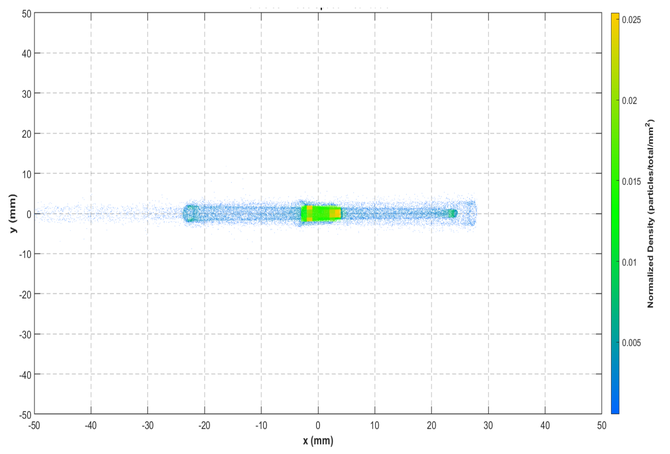

Fig. 2: In 4μs mode, particle density distribution (43.5 MeV, 111 mA)

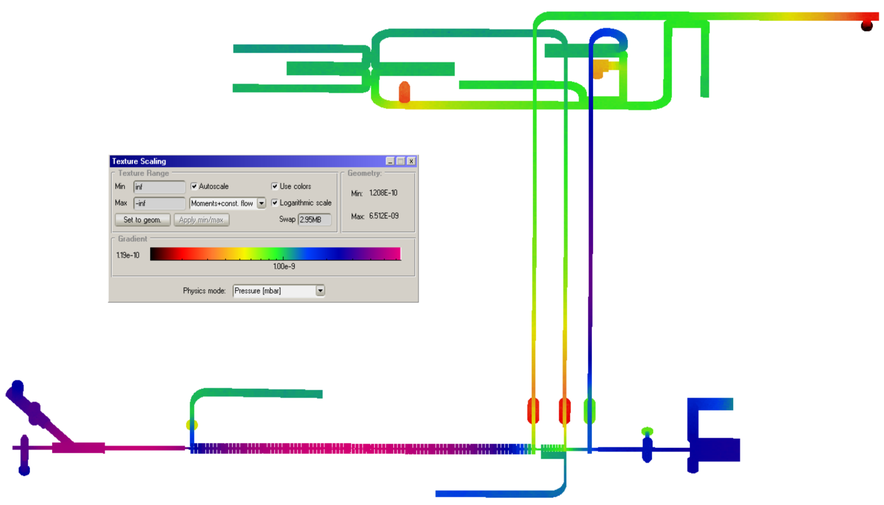

Fig. 3: Vacuum Distribution Calculation Diagram

Fig. 4: Titanium window

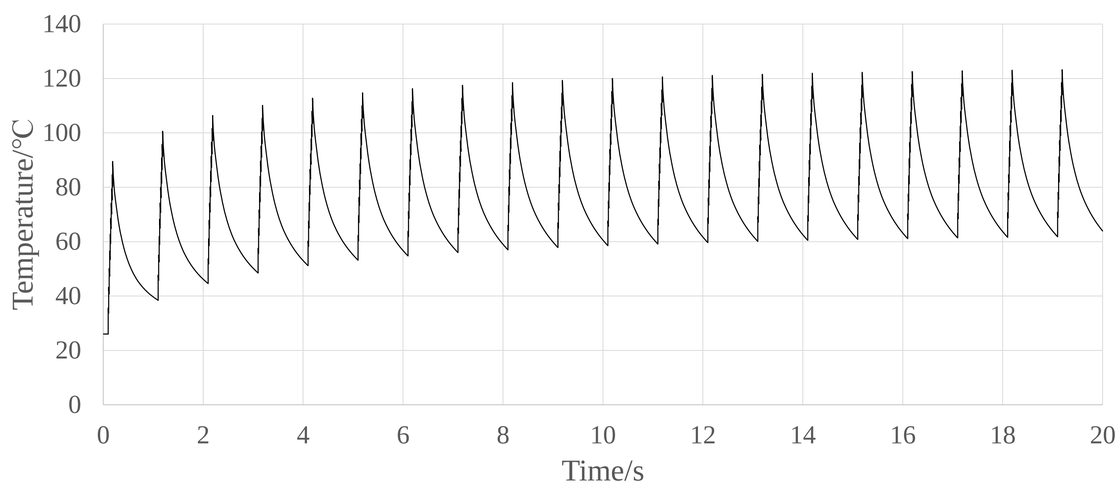

Fig. 5: Change in the central temperature of titanium windows

Project two

The project involves setting up a linear high-power test bench for accelerating tubes, spherical energy storage cavity energy multipliers, and the like. It requires a vacuum level better than 1.0e-5 Pa when increasing power.

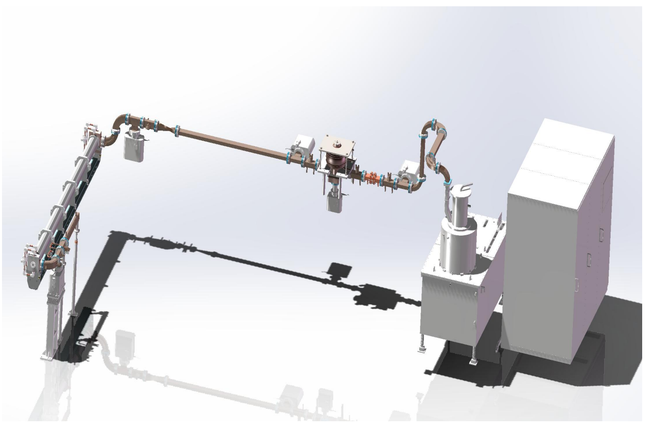

Fig. 6: Assembly drawing

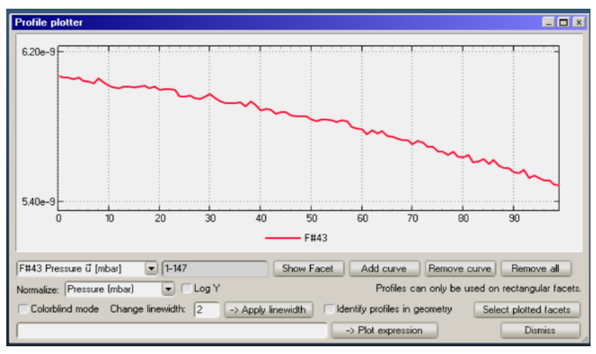

Fig. 7: Pressure curve

Fig. 8: Actual product image

Project three

The project, based on the actual design layout of HEPS's high-energy transport line, has built an offline vacuum system test bench to simulate the actual vacuum distribution.

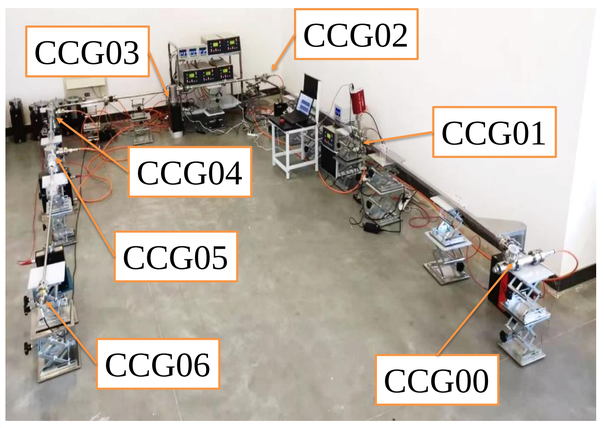

Fig. 9: Actual product image

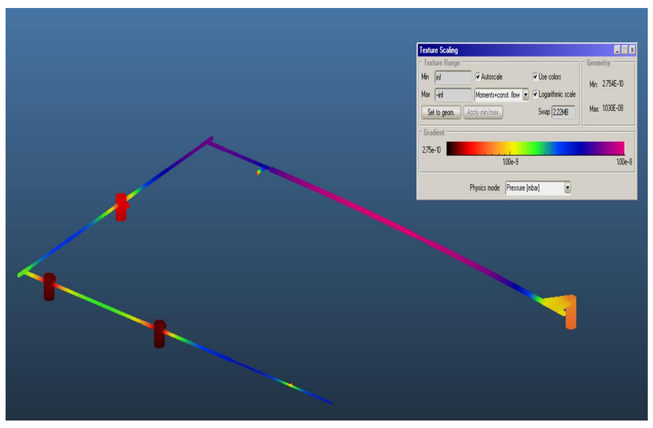

Fig. 10: Pressure distribution map

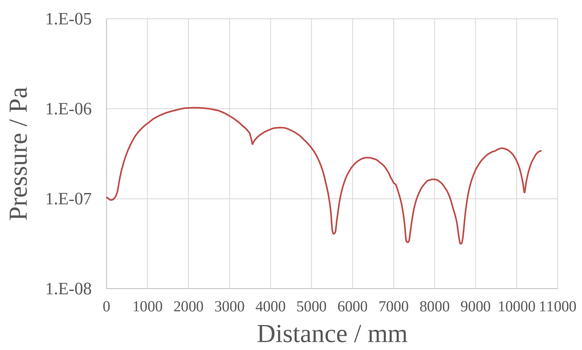

Fig. 11: Calculation curve of vacuum state at the middle section

Table 2: Comparison between simulated and measured values

Name	Calculated value/Pa	Measurement value/Pa
CCG00	1.02-7	2.8e-7
CCG01	9.7e-6	8.5e-7
CCG02	6.16e-7	5.3e-7
CCG03	4.29e-8	7.4e-8
CCG04	3.41e-8	6.8e-8
CCG05	3.32e-8	7.2e-8
CCG06	3.46e-7	2.2e-6

中国科学院高能物理研究所
Institute of High Energy Physics, Chinese Academy of Sciences

A02

The Application of Vibration Wire Measurement Technology in Pre-alignment Unit of HEPS Storage Ring

Luping Yan[1], Lan Dong[12], Tong Wang [12] , Xiaolong Wang [12], Yuanying Han [1], Xiaoyang Liu [1], Luyan Zhang [1], Haoyue Yan [1], Shang Lu [1]

1. Institute of High Energy Physics, ChineseAcademy of Sciences, Beijing, 100049, China

2. Dongguan Neutron Science Center, Dongguan 523803, China

Luping Yan, IHEP
yanluping@ihep.ac.cn

Abstract

The High Energy Photon Source (HEPS), China's first fourth-generation synchrotron light source, requires a pre-alignment precision of 0.03 mm between unit magnets in the storage ring pre-alignment units. This poster presents the 3-magnet and 5-magnet unit structures of the HEPS storage ring, where the vibrating wire technique is employed for magnetic center measurement. A laser displacement system has been developed to enhance sag correction accuracy. Experimental results demonstrate that the fitting deviations of both standard unit types are better than 0.015 mm, meeting the pre-alignment precision requirements.

Introduction

The storage ring of HEPS has a circumference of approximately 1.3 km and consists of 288 pre-alignment standard units, including 96 three-magnet units, 96 five-magnet units and 96 eight-magnet units. the alignment accuracy between magnets in the pre-alignment units is a critical technical indicator for ensuring long-term stable and efficient operation of the storage ring. Currently, multi-laser systems are used for magnetic center pre-alignment in the HEPS storage ring pre-alignment units. To ensure the reliability and accuracy of this high-precision measurement system, it is essential to introduce vibration wire technology as an independent high-precision measurement system for verifying the alignment accuracy of the pre-alignment units.

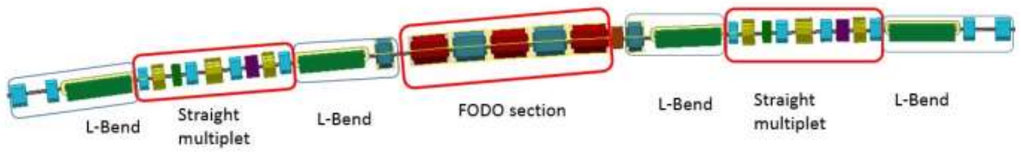

Layout of a standard unit equipment

Principle

Vibration wire magnetic center measurement technology involves scanning vibration wire in both horizontal and vertical directions near the approximate magnetic center of a magnet to detect the magnetic field distribution and determine the magnetic center position. The relationship between the magnetic field components of a quadrupole magnet and their deviation from the magnetic center is given by:

$$B_y = G(x - x_0)$$
$$B_x = G(y - y_0)$$

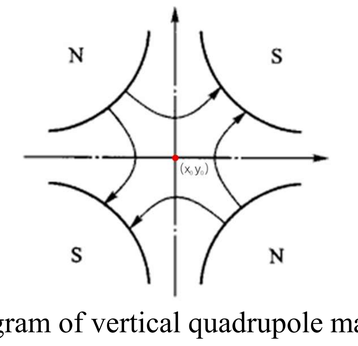

Diagram of vertical quadrupole magnetic field

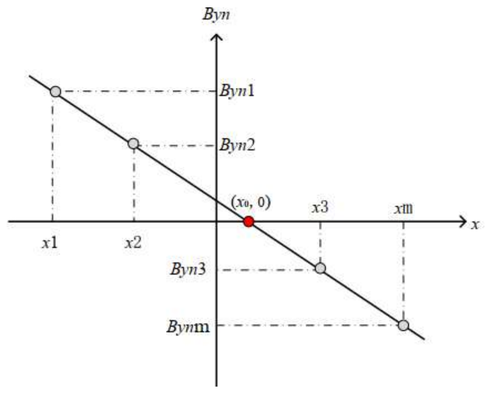

Schematic of horizontal magnetic center measurement method for quadrupole magnets

Three-magnet unit

The selected pre-alignment three-magnet unit R29DQ1 consists of 2 quadrupole magnets and 1 corrector magnet. The corrector magnet is used to correct beam deviations from the orbit. Mechanical center calibration can meet alignment accuracy requirements, so it is not included in the scope of this vibration wire magnetic center verification measurement.

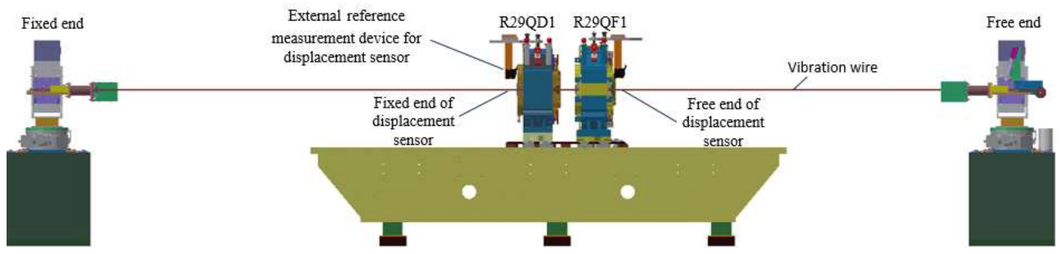

The pre-alignment three-magnet unit vibrating-wire scanning schematic diagram

Magnet types	Measurement times/times	Fixed end		Free end	
		x /mm	y/mm	x/mm	y/mm
R29QF1	1	-0.031	-0.326	-0.038	-0.329
	2	-0.038	-0.340	-0.038	-0.335
	Deviation/mm	0.007	0.015	0.000	0.006
R29QD1	1	-0.026	-0.339	-0.028	-0.342
	2	-0.032	-0.340	-0.032	-0.340
	Deviation/mm	0.006	0.001	0.004	0.002

Repeatability result of vibrating-wire magnetic center scanning in pre-alignment three-magnet unit

Vibration wire fixation method	Magnet entrance and exit	Horizontal x/mm	Vertical y/mm	Longitudinal z/mm
Fixed end	R29QF1EN	0.000	0.000	0.0
Free end	R29QF1EX	0.000	0.000	246.0
Fixed end	R29QD1EN	0.005	-0.004	445.0
Free end	R29QD1EX	0.008	-0.006	639.0

Vibrating-wire scanning results of the pre-alignment three-magnet unit in the HEPS storage ring

Five-magnet unit

The selected pre-alignment five-magnet unit R29FD1 consists of 4 quadrupole magnets and 1 corrector magnet.

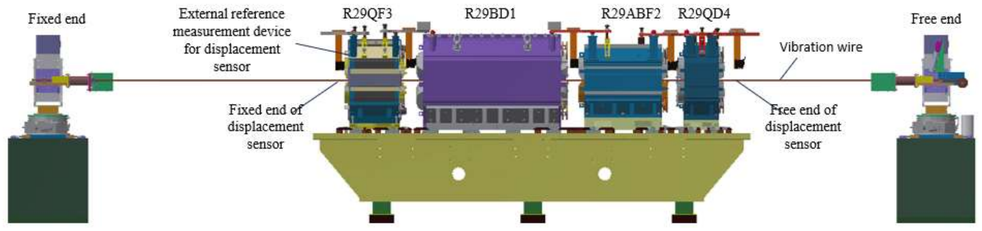

The pre-alignment five-magnet unit vibrating-wire scanning schematic diagram

Magnet types	Measuremen t times/times	Fixed end		Free end	
		x/mm	y/mm	x/mm	y/mm
R29QF3	1	0.003	-0.019	0.006	-0.022
	2	0.003	-0.017	0.004	-0.017
	Deviation/mm	0.000	-0.002	0.002	-0.005
R29BD1	1	0.003	0.125	0.006	0.126
	2	0.003	0.128	0.004	0.127
	Deviation/mm	0.000	-0.003	0.002	-0.001
R29ABF2	1	0.005	0.099	0.006	0.099
	2	0.005	0.099	0.006	0.099
	Deviation/mm	0.000	0.000	0.000	0.000
R29QD4	1	0.004	-0.049	0.002	-0.047
	2	0.001	-0.051	0.001	-0.051
	Deviation/mm	0.003	0.002	0.001	0.004

Repeatability result of vibrating-wire magnetic center scanning in pre-alignment three-magnet unit

Vibration wire fixation method	Magnet entrance and exit	Horizontal x/mm	Vertical y/mm	Longitudinal z/mm
Fixed end	R29QF3EN	0.004	-0.002	0.000
Free end	R29QF3EX	0.003	-0.002	375.000
Fixed end	R29BD1EN	-0.007	-0.001	633.920
Free end	R29BD1EX	-0.003	-0.002	1 674.920
Fixed end	R29ABF2EN	0.000	0.011	1 869.720
Free end	R29ABF2EX	0.002	0.009	2 460.720
Fixed end	R29QD4EN	0.002	-0.007	2 674.120
Free end	R29QD4EX	0.000	-0.007	2 935.120

Vibrating-wire scanning results of the pre-alignment five-magnet unit in the HEPS storage ring

Laser displacement system-Repeatability

The working principle of a laser displacement sensor involves emitting a laser beam onto the surface of the measured object and receiving the reflected light signal to calculate the distance.

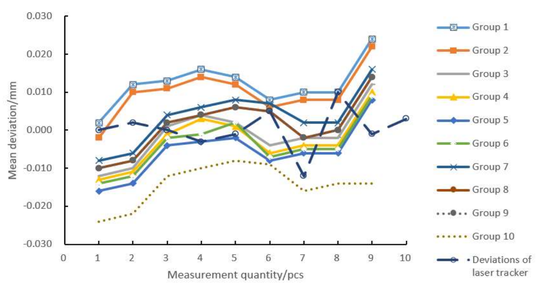

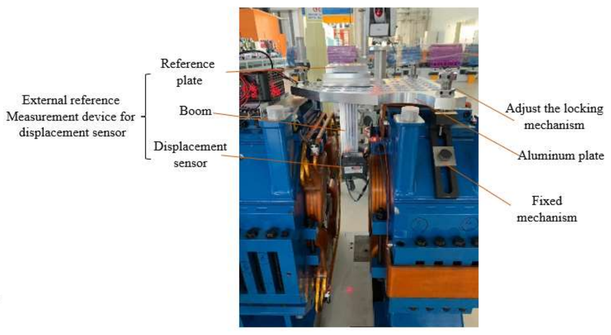

Repeatability test results of external reference for laser displacement sensor

Laser displacement system-Compare

Magnet types	Longitudinal/mm	Sag/mm
R29QF1	229	-0.017
R29QD1	648	-0.014

Magnet types	Longitudinal /mm	Sag/mm
R29QF3	296.83	-0.055
R29BD1	1 138.69	-0.196
R29ABF2	2 298.93	-0.157
R29QD4	2 920.68	-0.025

Wire sag of three-magnet and five-magnet units

Wire position	Longitudinal z/mm	Sag of conductor obtained by two methods/mm		Deviation /mm
		Fundamental frequency method	Displacement sensor fitting method	
Fixed end	0.0	0.000	0.000	0.000
Mid of R29QF1	229.0	-0.010	-0.017	-0.007
Mid of unit	423.0	-0.012	-0.021	-0.009
Mid of R29QD1	648.0	-0.008	-0.014	-0.006
Free end	828.0	0.000	0.000	0.000

Comparison of Sag obtained by two methods

Poster ID :61The 2025 International Workshop on the High Energy Circular Electron Positron Collider (CEPC2025), GuangZhou, China, Nov 5-10, 2025

A03

中国科学院高能物理研究所
Institute of High Energy Physics, Chinese Academy of Sciences

SAD-Based Particle Tracking Simulation of Injection Efficiency and Beam Loss in SuperKEKB LER

Mingyang Zhao*, Meng Li, Philip Bambade, Dou Wang*, Jie Gao
Institute of High Energy Physics, Chinese Academy of Sciences, Beijing 100049, China

Abstract

This study employs the SAD program to perform particle tracking simulations of the multi-turn injection process in the SuperKEKB Low-Energy Ring (LER). By tracking large numbers of particles, we quantitatively analyze the beam loss distribution and identify the primary sources of particle loss during injection. The results provide a detailed understanding of the factors limiting the injection efficiency and offer insights for optimizing the injection parameters to mitigate beam loss.

Introduction

Particle colliders, such as SuperKEKB, push the frontiers of high-energy physics by pursuing unprecedented luminosities. This endeavor critically depends on the efficient and continuous injection of particle beams to replenish those lost due to collisions and other effects. In this study, we employ the SAD (Strategic Accelerator Design) program to perform high-fidelity, multi-turn particle tracking simulations of the injection process into the SuperKEKB LER. The primary objectives are to quantitatively analyze the beam loss distribution around the ring and pinpoint the key factors limiting the injection efficiency.

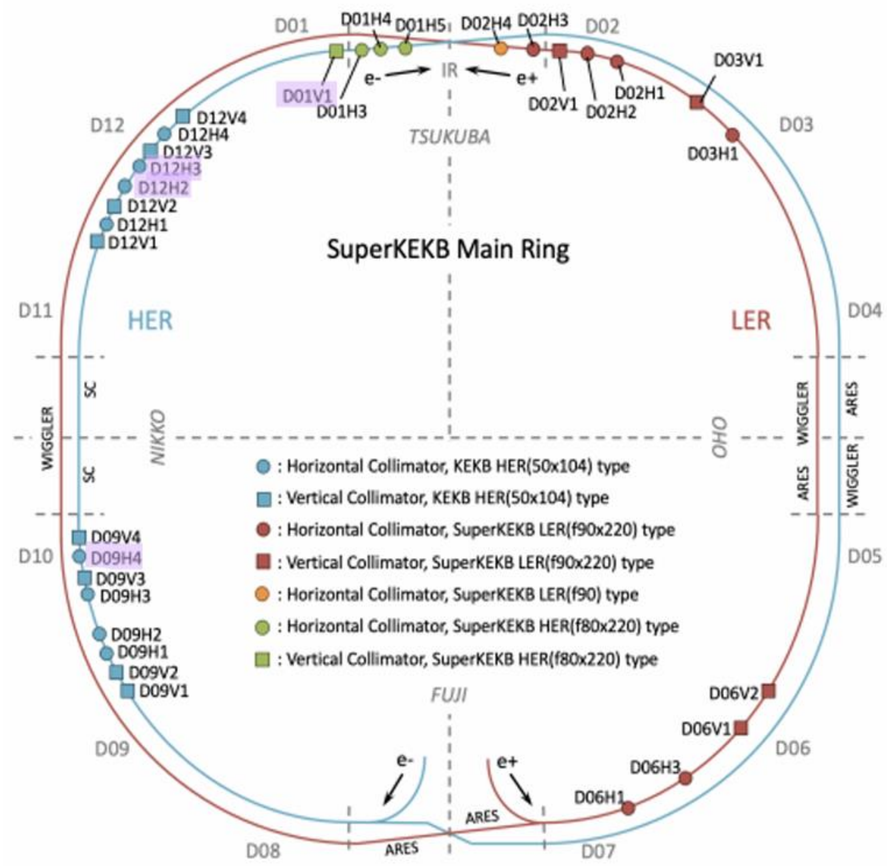

The SuperKEKB Main Ring

Simulation Setup

- To accurately simulate beam loss and particle tracking in the SuperKEKB LER, a detailed aperture model is implemented in SAD, defining collimator aperture.

```
APERT  AQC1LC  =(AX =.01 AY =.0135 DY =.0015 )
       AQC1LO  =(AX =.013     AY =.0135 DY =.0015 )
       AQC2LC  =(AX =.035     AY =.035  DY =.0015 )
       AQC2LO  =(AX =.035     AY =.035  DY =.0015 )
       PMD06H1 =(AX =1    AY =1 )
       FPMD06H2=(AX =1    AY =1 )
       PMD06H3 =(DX1 =.00992  DX2 =-.01015  DY1 =.05     DY2 =-.05     AX =1   AY =1 )
       FPMD06H4=(DX1 =.00996  DX2 =-.00994  DY1 =.05     DY2 =-.05     AX =1   AY =1 )
       PMD06V1 =(DX1 =.05     DX2 =-.05     DY1 =.00246  DY2 =-.00222  AX =1   AY =1 )
       PMD06V2 =(DX1 =.05     DX2 =-.05     DY1 =.00209  DY2 =-.00328  AX =1   AY =1 )
       PMD03H1 =(DX1 =.00997  DX2 =-.01003  DY1 =.05     DY2 =-.05     AX =1   AY =1 )
       FPMD03H2=(AX =1    AY =1 )
       PMD03V1 =(AX =1    AY =1 )
       FPMD03V2=(AX =1    AY =1 )
       PMD02H1 =(DX1 =.00788  DX2 =-.00790  DY1 =.05     DY2 =-.05     AX =1   AY =1 )
       PMD02H2 =(DX1 =.01037  DX2 =-.01081  DY1 =.05     DY2 =-.05     AX =1   AY =1 )
       PMD02V1 =(DX1 =.05     DX2 =-.05     DY1 =.00063  DY2 =-.00147  AX =1   AY =1 )
       PMD02H3 =(DX1 =.01481  DX2 =-.01474  DY1 =.05     DY2 =-.05     AX =1   AY =1 )
       PMD02H4 =(DX1 =.00745  DX2 =-.00742  DY1 =.05     DY2 =-.05     AX =1   AY =1 )
       AQC2RO  =(AX =.035     AY =.035  DY =.001 )
       AQC2RC  =(AX =.035     AY =.035  DY =.001 )
       AQC1RO  =(AX =.013     AY =.0135 DY =.001 )
       AQC1RC  =(AX =.01 AY =.0135 DY =.001 )
```

Collimator Aperture

- The number of initial particles is 5,000, and the particle distribution adopts Gaussian distribution (with a value of three times σ).
  N=5000 GCUT=3 x offset = -0.0076 m= -7.6 mm

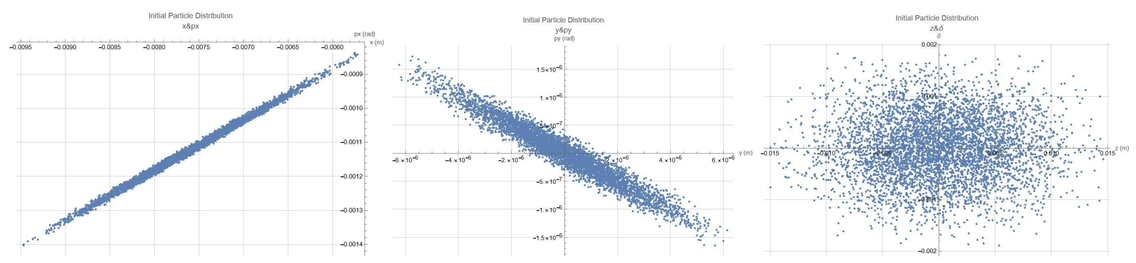

Initial Particle Distribution

Injection simulation of LER

Track 5000 particles 1000 turns
The comparative analysis reveals that collimators significantly accelerate initial particle loss by defining strict machine acceptance, while the inclusion of beam-beam interactions further exacerbates particle loss, particularly for beams with larger horizontal emittance.

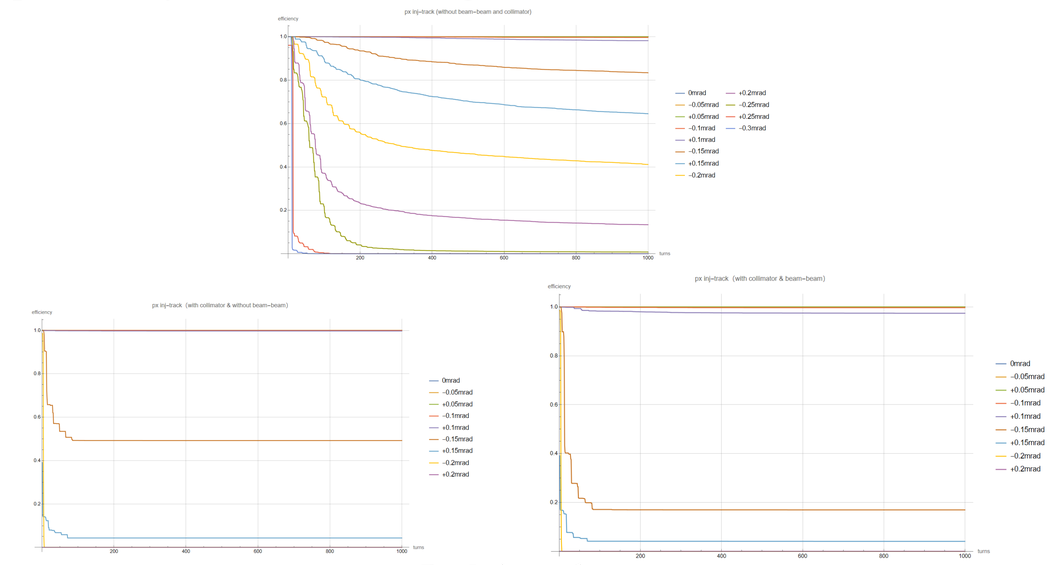

Px Inj-track

For all parameters (p_x, p_y, y, δ), efficiency peaks at *"optimal" values* (e.g., p_x=0, p_y=0, y=0, δ=0) and decreases with deviation. Collimators and beam-beam interactions (seen in *green*/*orange* curves) narrow the "range of high efficiency" — this reflects how these components influence the beam loss during injection.

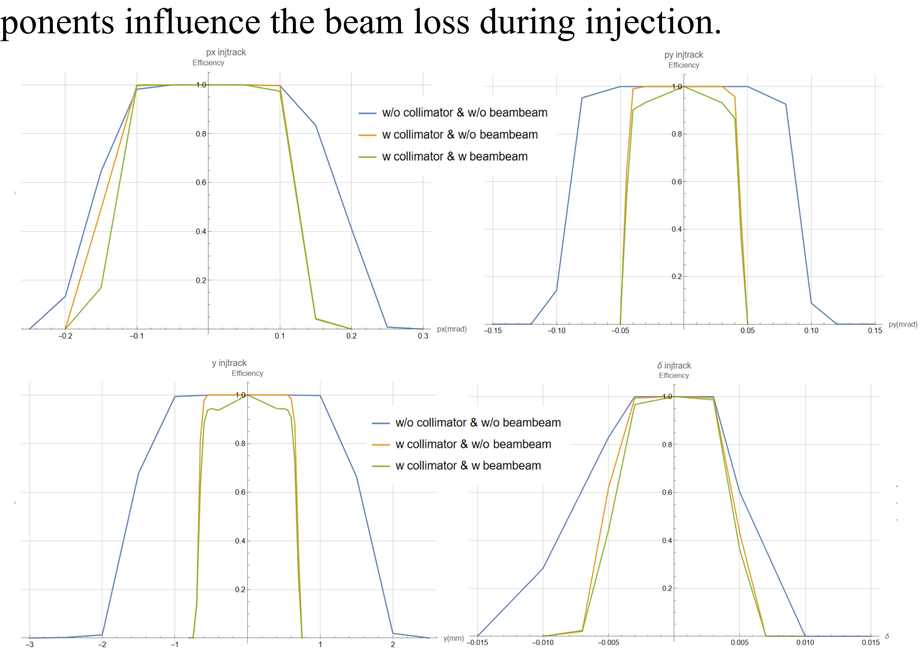

Integrated with Collimator & Beam-Beam Comparison

Beam Loss Distribution

With collimators in place, the majority of beam loss occurs at the PMD02V1 and PMD02H4; without collimators, the majority of beam loss occurs at the AQC1RO and AQC1LC. We can see the collimators are effective in protecting the IR region.

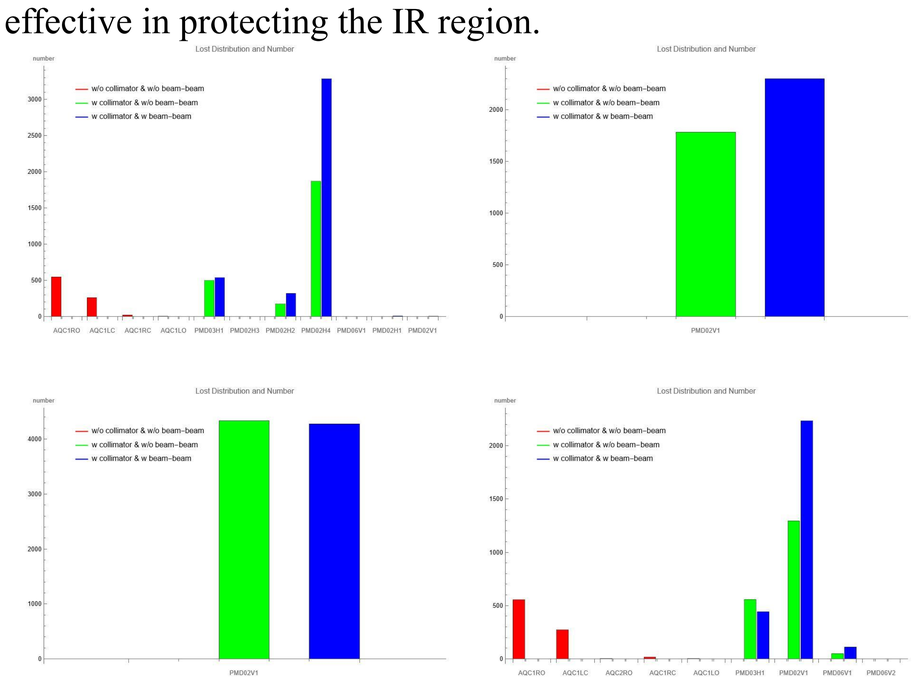

Beam Loss Distribution & Number

zhaomy@ihep.ac.cn

STUDY ON BEAM VACUUM LEAK DETECTION METHOD FOR HEPS STORAGE RING

A04

Liu Tianfeng，Guo dizhou，Dong Haiyi，Liu Baiqi，Zhang Lei， Li Qi, Tian Pilong, Huang Tao, Yang Qi, Ma Yongsheng, Sun Fei, Sun Xiaoyang, Zhu Bangle

Email:liutf@ihep.ac.cn

Institute of High Energy Physics, Chinese Academies of Sciences, Beijing, China

Introduction

As a major national science and technology infrastructure, the High Energy Photon Source (HEPS) imposes extremely high requirements on the vacuum level and c leanliness of its beam vacuum system. Such strict vacuum environment presents unprecedented challenges to the manufacturing, installation, connection and leak detect ion processes of all system components. Any tiny leak or material outgassing may deteriorate the vacuum level, thereby affecting the beam lifetime and the performanc e of the light source.

The vacuum leak detection strategies and practices adopted in the HEPS storage ring vacuum system during installation, commissioning and operation phases provi de a solid guarantee for the system to meet standards and operate stably.

HEPS Vacuum Equipment Layout

HEPS is composed of 48 standard cells: straight sections and bending sections.

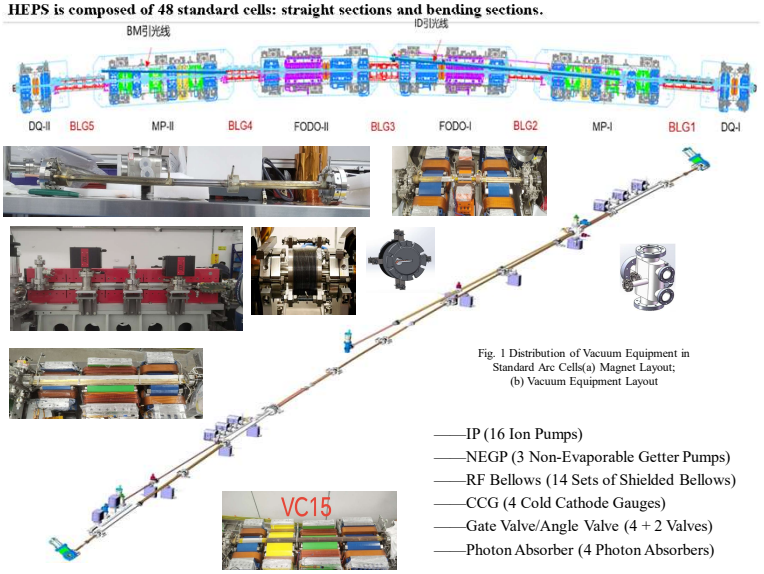

Fig. 1 Distribution of Vacuum Equipment in Standard Arc Cells(a) Magnet Layout; (b) Vacuum Equipment Layout

——IP (16 Ion Pumps)
——NEGP (3 Non-Evaporable Getter Pumps)
——RF Bellows (14 Sets of Shielded Bellows)
——CCG (4 Cold Cathode Gauges)
——Gate Valve/Angle Valve (4 + 2 Valves)
——Photon Absorber (4 Photon Absorbers)

Calculation of Storage Ring Pressure Distribution

1.Stainless steel vacuum chambers VC02, VC04, VC14 and VC17: Gas is mainly pumped by ion pumps and getter pumps.
2.Chromium-zirconium-copper vacuum chambers: The inner surface is coated with a getter film (accounting for approximately 70% of the total length).
3.Through calculation, it is found that the positions coated with the getter film provide a lower pressure.
4.Causes of pressure increase in the vacuum system:
① Thermal outgassing of vacuum materials;
② Photon desorption mainly caused by synchrotron radiation light striking the inner surface of the vacuum chamber.

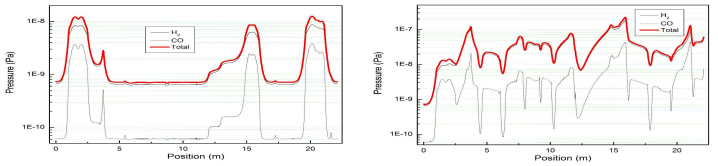

Fig. 2. Static/Dynamic Pressure Distribution Diagram of the Storage Ring Standard Arc Cell

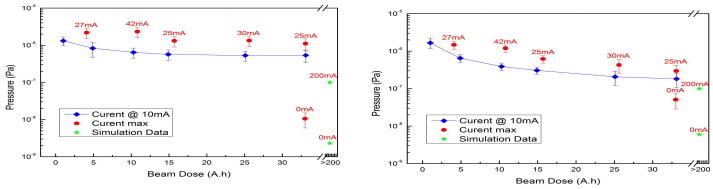

Fig. 3 Curve of the Relationship Between Beamline Vacuum Level and Beam Current

Leak Detection Schemes and Equipment

1. Leak Detection During Installation

The system is in a high-vacuum state during this phase. A helium mass spectrometer leak detector is mainly used for leak detection. The leak detector is connected via a metal bellows to the installed and to-be-tested section of the vacuum system. Helium gas is sprayed on suspected leak locations; if a leak exists, the helium gas will enter the leak detector and be detected. This method features high sensitivity and can accurately locate the position of leaks. The leak detection process is shown in the figure.

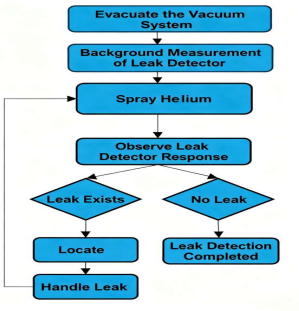

Fig. 4 Process flow chart of helium mass spectrometer leak detection

2. Leak Detection After Baking of the Vacuum System

The system is in a high-vacuum state. A quadrupole mass spectrometer installed on the system is used for leak detection.

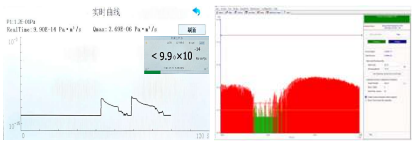

Fig. 5 Main interface of the leak detector

Meanwhile, by monitoring the full spectrum or the partial pressure of specific mass numbers, the quadrupole mass spectrometer can accurately identify key gases such as H_2, He, H_2O, N_2, O_2, and CO_2, which is used for residual gas analysis.

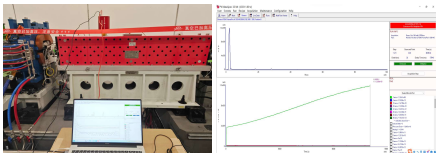

Fig. 6 Gas composition measurement by quadrupole mass spectrometer

Installation and Leak Detection

During the installation and commissioning of the HEPS storage ring, various types of leak points were encountered. Below, combined with typical cases, the characteristics and solutions of various leaks are analyzed.

1.Seal Gasket Installation Issues

Improper installation of seal gaskets at flange joints is the most common cause of leaks in vacuum systems. In the early stage of HEPS vacuum system installation, flange joints often exhibited leaks of varying degrees. Most of these leaks could be resolved by further tightening the flange bolts, while a small number of joints required seal gasket replacement.

2.Outgassing from Material Surfaces

Outgassing through micro-pores on material surfaces is a relatively concealed type of leak in vacuum systems. During the HEPS project, surface outgassing was detected at one stainless steel adapter. The leak detector showed that the leak rate increased slowly over time, typically reaching the maximum leak rate within 2–5 minutes.

Treating outgassing:

For minor outgassing that does not affect the ultra-high vacuum, the temporary method of brushing vacuum sealant is adopted.

For areas with significant outgassing, the vacuum components need to be replaced during system maintenance.

Tab.1 Leak Types and Treatment Solutions for the HEPS Vacuum System

Leak Type	Leak Detector Response Characteristics	Location Method and Process	Solution
Improper Seal Gasket Installation	Rapid response after helium spraying, slow leak rate decrease.	Spray helium on flange connections, with obvious response.	Retighten bolts; if leak rate meets standards, pass; if ineffective, replace the seal gasket.
Material Surface Outgassing	Slow increase in the leak detector’ s background leak rate.	Use the alcohol coating method for auxiliary judgment.	Temporarily seal with vacuum glue and replace later.
Ion Pump High-Voltage Head Leak	Slow leak rate increase; rapid leak detector response when helium is sprayed on the high-voltage head.	Power off the ion pump, remove the high-voltage head, and spray helium.	Replace the ion pump.
Ion Pump Shell Leak	Obvious leak rate increase when helium is sprayed near the ion pump.	Remove the ion pump shell and accurately locate the leak point.	Replace the ion pump if it does not affect system operation.
Weld Defect	Slow leak rate increase about 3-5 minutes after helium spraying.	Perform hood leak detection on the weld.	Repair the weld by welding

Conclusions

Through the practice of leak detection and gas analysis throughout the entire process of the HEPS storage ring vacuum system, from installation to operation, the following conclusions can be drawn:

1.Effectiveness of Leak Detection Strategy: The phased leak detection strategy, which combines a helium mass spectrometer leak detector and a quadrupole mass spectrometer (QMS), has proven to be efficient and reliable. The characteristics and disposal plans summarized for six types of typical leak points hold significant reference value for leak detection work in similar large-scale vacuum engineering projects.

2.System Performance Meets Standards: The adopted leak detection and quality control methods have successfully ensured that the HEPS storage ring vacuum system achieves and maintains the extremely high vacuum level and cleanliness required by the design, laying a solid foundation for the successful commissioning and operation of HEPS.

In the future, we will continue to use the Quadrupole Mass Spectrometer (QMS) for long-term monitoring of gas composition changes in the vacuum system, conduct in-depth research on gas load patterns under different operating modes, and provide continuous data support for the performance optimization and reliable operation of HEPS.

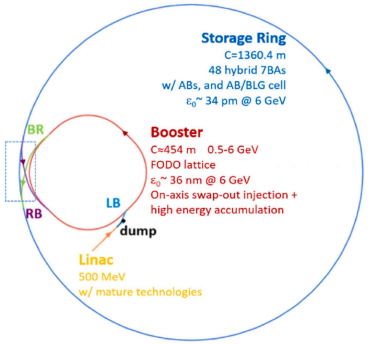

Fig. 7 Schematic Diagram of HEPS Project Layout

References： Dong H Y， He P， Li Q et al. Vacuum system of the HEPS storage ring[J]. Vacuum，2025，62(2)：1-11.

Poster ID: 93 The 2025 International Workshop on the High Energy Circular Electron Positron Collider (CEPC2025), GuangZhou, China, Nov 5-10, 2025

Measurement of 3D distance from JUNO Detector to Nuclear Power Reactors

A05

Xiaoyang Liu[1], Tong Wang[1,2], Lan Dong[1], Shang Lu[1], Bo Li[1,2], Na Ma[1,2]
Xiaolong Wang[1], Lingling Men[1], Jing Liang[1,2]

Institute of High Energy Physics, Chinese Academy of Sciences, Beijing 100049, China[1]
Spallation Neutron Source Science Center, Dongguan 523803, China[2]

Abstract: The primary goal of JUNO is to determine the mass hierarchy of neutrinos. Accurate measurement of the distance from JUNO detector to nuclear power reactors is essential for providing relevant parameters necessary for the physical analysis of the neutrino experiment. This paper provides a detailed introduction to the 3D measurement plan from the JUNO detector to the Yangjiang and Taishan nuclear power reactors. It describes the main components of the measurement process, including GNSS measurements, total station measurements, and laser tracker measurements. Additionally, the data processing methods and results are analyzed to accurately determine the three-dimensional spatial distance from the detector to the nuclear power reactors.

Key words: JUNO Detector, Nuclear Power Reactor, Distance Measurement, Data Processing

Introduction

JUNO is the world's first next-generation large-scale neutrino experimental facility. Its primary goal is to determine the mass hierarchy of neutrinos. The execution of the experiment requires determining the three-dimensional distances from JUNO detector to nuclear power reactors.

As shown in Fig.1, the positional relationships between the control network of Yangjiang and Taishan nuclear power plants and the nuclear reactors, as well as between the control network of experimental hall and the central detector, are known. First, GNSS measurements are conducted on the control network points of JUNO, Yangjiang and Taishan Nuclear Power Plants to determine their positional relationships. Subsequently, using measurement technologies such as total station and laser tracker, joint measurements are taken through inclined shaft and tunnel to link the control network of JUNO site with the experimental hall. Through a series of data processing steps, the positional relationship between the nuclear reactors and the central detector is ultimately determined, and their distances are calculated.

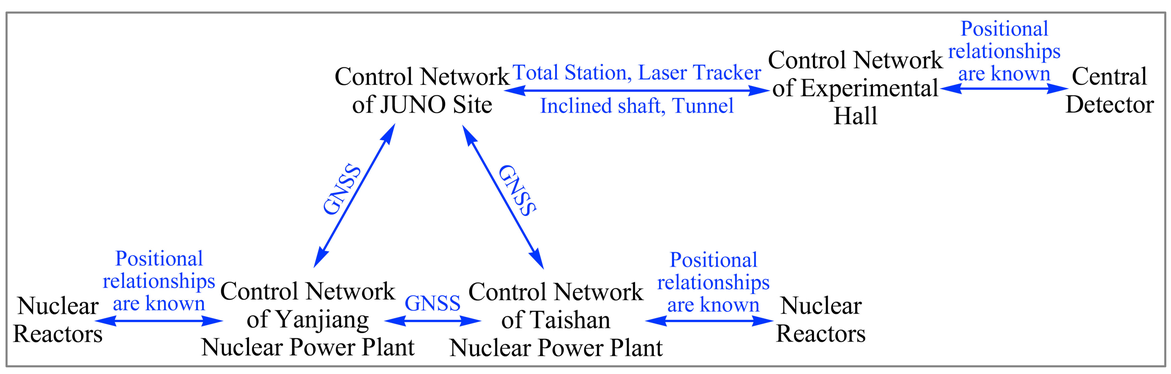

Fig.1 Positional relationship between the central detector and the nuclear reactors

Measurement and Data Processing

GNSS Measurement: A total of 12 Leica GNSS receivers were used to simultaneously observe 13 points across the three locations, with observations conducted over three time periods, each lasting more than 8 hours. The GNSS measurement network configuration is shown in Fig.2.

GNSS Data Processing: The observation data from the three locations and three time periods were processed using Leica Geo Office software for combined adjustment calculations, utilizing broadcast ephemeris for unconstrained adjustment. The adjustment coordinate error components are shown in Fig.3, with an overall point accuracy of ±3.3mm.

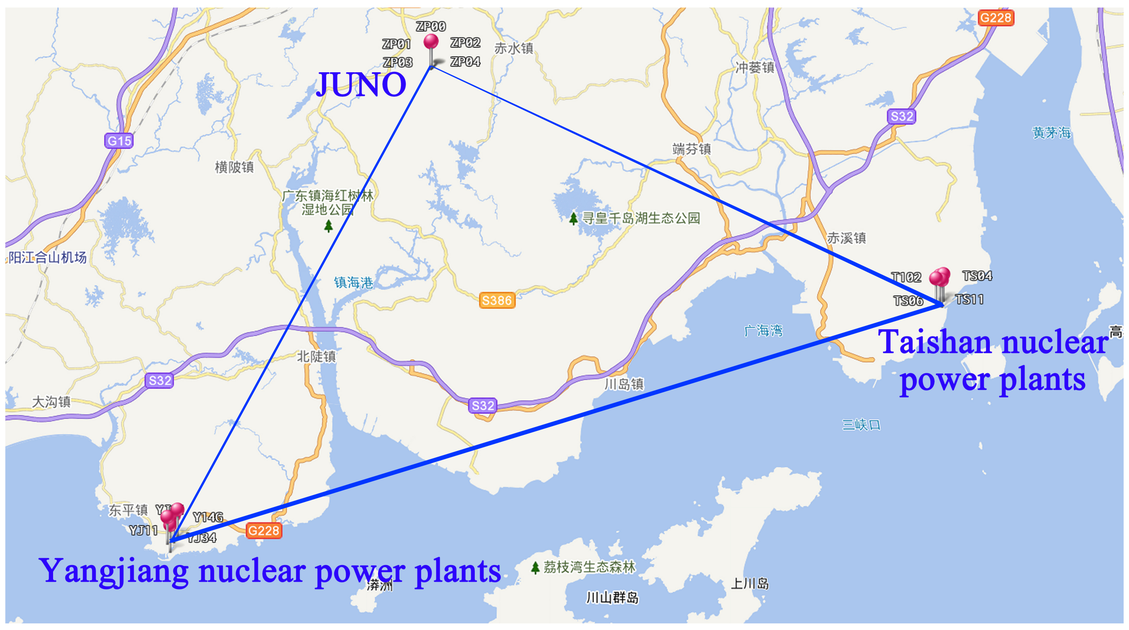

Fig.2 GNSS measurement network configuration

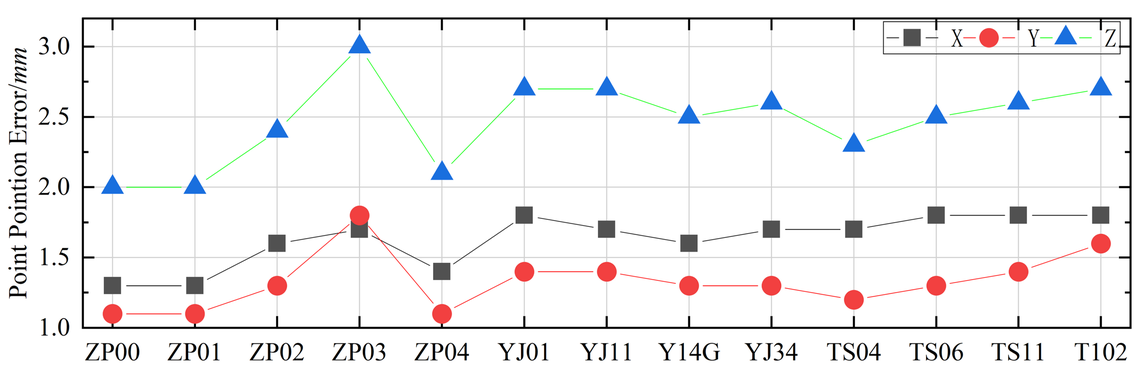

Fig.3 Adjustment residual of GNSS network

Total Station Measurement: The TM50i total station was used to conduct joint measurements between the neutrino site control network and the control points set at the bottom of the inclined shaft. The measurement network is illustrated in Fig.4, featuring a tightly arranged double wire network to improve measurement accuracy.

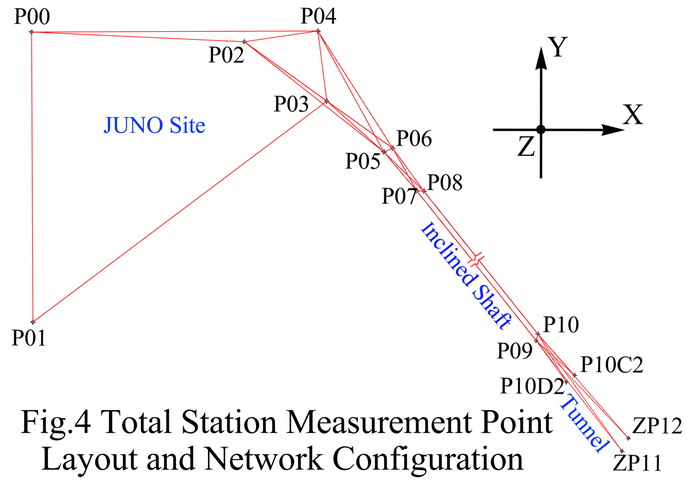

Fig.4 Total Station Measurement Point Layout and Network Configuration

Total Station Measurement Data Processing: The COSA adjustment software was used to conduct adjustment calculations on the planar and elevation data measured by the total station. The adjustment coordinate error components are shown in Fig.5. The maximum point accuracy is 3.8 mm.

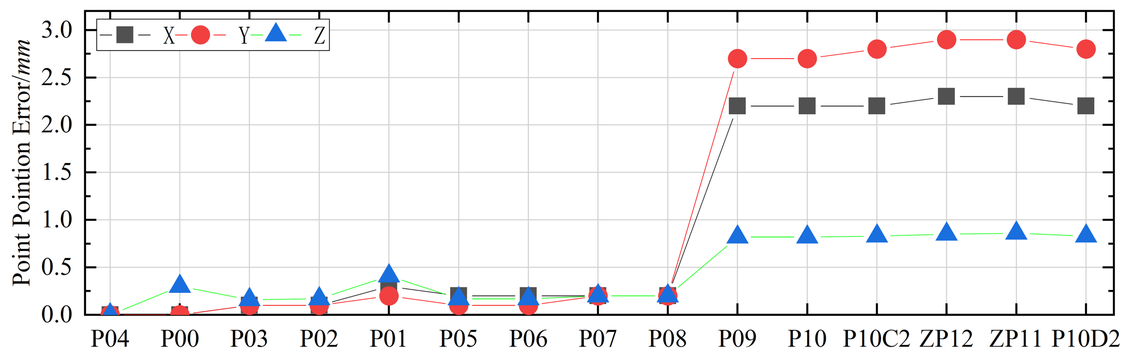

Fig.5 Adjustment residual of total station network

Laser Tracker Measurement: The Leica AT403 laser tracker was used to conduct joint measurement of the control network in the tunnel and experimental hall. The measurement network is shown in Fig.6.

Laser Tracker Measurement Data Processing: The Unified Spatial Metrology Network (USMN) function of the SpatialAnalyzer software was used for adjustment. The adjustment results are shown in Fig.7, with a maximum point deviation of 1.46 mm and a standard point deviation of 0.15 mm.

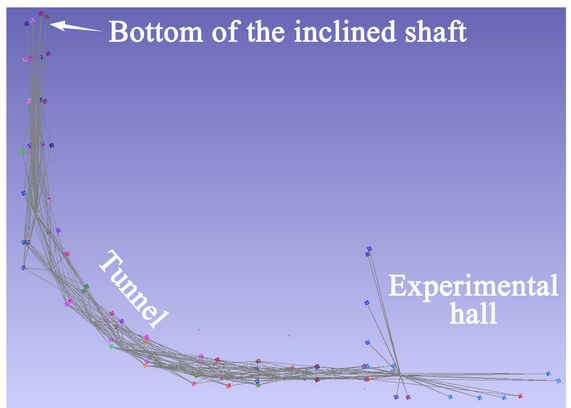

Fig.6 Laser tracker measurement network

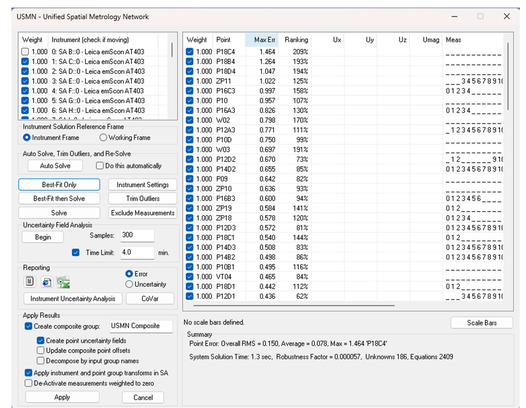

Fig.7 Adjustment results of USMN function

Results

Due to the inconsistency in coordinate systems among the adjustment results from GNSS, total station, and tracker measurements, the BestFit software was used to perform a fitting transformation using common points among them, unifying all coordinate results into a single coordinate system.

Based on the coordinate results, the distance between JUNO detector and nuclear power reactors was calculated, as shown in Tab.1.

Tab.1 Distance between JUNO detector and nuclear power reactors

Reactor Name	Distance/m
YJ1#	52737.411
YJ2#	52823.926
YJ3#	52407.402
YJ4#	52493.887
YJ5#	52106.712
YJ6#	52193.170
TS1#	52766.123
TS2#	52636.353
TS3#	52329.069
TS4#	52202.361

Conclusion

This paper provides a detailed introduction to the 3D measurement plan from the JUNO detector to the Yangjiang and Taishan nuclear power reactors. It describes the main components of the measurement process, including GNSS measurements, total station measurements, and laser tracker measurements. Additionally, the data processing methods and results are analyzed to accurately determine the three-dimensional spatial distance from the detector to the nuclear power reactors.

† email address: liuxiaoyang@ihep.ac.cn

Poster ID :91The 2025 International Workshop on the High Energy Circular Electron Positron Collider (CEPC2025), GuangZhou, China, Nov 5-10, 2025

Analysis of absolute position alignment and absolute position deviation of the high energy photon source storage ring tunnel

A06

Yan Haoyue[1]，Dong Lan[1]，Wang Xiaolong[1]，Wang Tong[1,2]，Liang Jing[1,2]，MaNa[1,2]，MenLngling[1]，Xuwen Dai[1]，Lu Shang[1]，Liu Xiaoyang[1]，Han Yuanying[1]，Yan Luping[1]，Zhang Luyan[1]，Li Bo[1,2]，He Zhenqiang[1,2]，Ke Zhiyong[1,2]

1.Institute of High Energy Physics, Chinese Academy of Sciences, Beijing 100049, China

2. Spallation Neutron Source Science Center, Dongguan 523803, China

Abstract: The design emittance of the High Energy Photon Source (HEPS) is ≤ 60 pm·rad, and its brightness reaches 1×10^{22} phs·s^{-1}·mm^{-2}·mrad^{-2}·(0.1%bw)$^{-1}$. This places higher demands on the absolute position accuracy of the storage ring equipment. To achieve the technical indicators of the HEPS and ensure smooth light emission, the accelerator alignment team precisely aligned the equipment of the 1360.4m circumference storage ring to its theoretical design position. The precise alignment of the storage ring ensures the position accuracy of the synchrotron radiation light emission equipment and provides a relatively smooth track under absolute position accuracy control for the efficient operation of the electron beam. In view of the narrow and long space inside the tunnel and the inability to have a wide field of view, to improve the absolute position measurement accuracy, a control network layout scheme based on precise measurement with a laser tracker and a dual-instrument synchronous measurement method were adopted. To reduce the systematic error of the instrument, the laser tracker used the double-sided measurement method for observation. Through displacement adjustment, the final alignment accuracy achieved a maximum deviation of 0.305mm and a standard deviation of 0.136mm for the absolute position of the storage ring unit magnets, both of which are better than the design indicators.

Key words: High Energy Photon Source; control network; laser tracker; alignment; precision analysis

INTRODUCTION

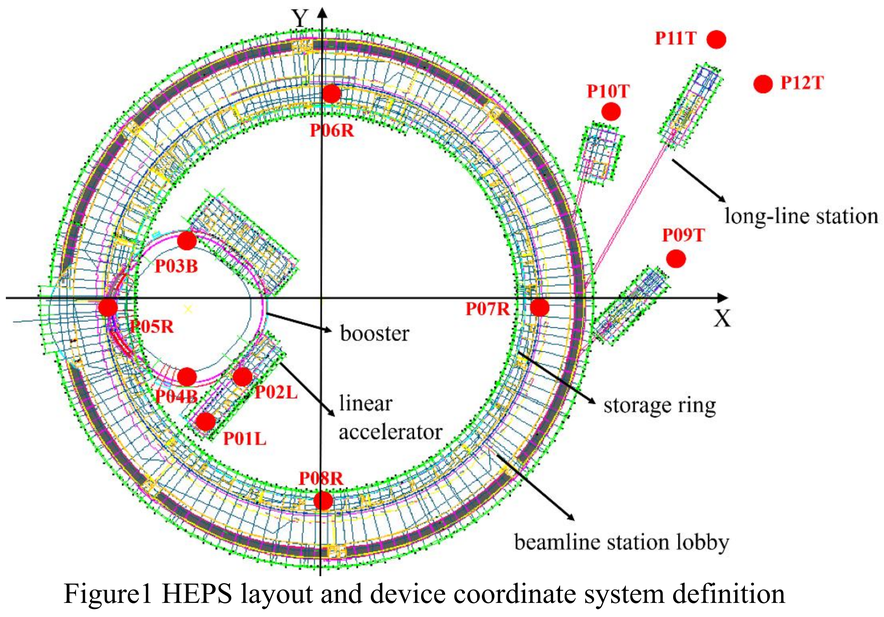

Figure1 HEPS layout and device coordinate system definition

The entire HEPS device consists of a linear accelerator,a booster, a storage ring, and beamline stations.

The storage ring has a circumference of 1,360.4 meters and is divided into 288 sections at intervals of approximately 6 to 8 meters. A total of 1,440 control points form the tunnel network.

For the control network coordinate system of the entire High Energy Photon Source (HEPS) facility, its origin is set at the center of the storage ring. The due north direction is defined as the Y - axis, the X - axis is perpendicular to the Y - axis, and the Z - axis indicates the elevation direction. The definition of the coordinate system for the entire facility is presented in Figure 1.

METHODS

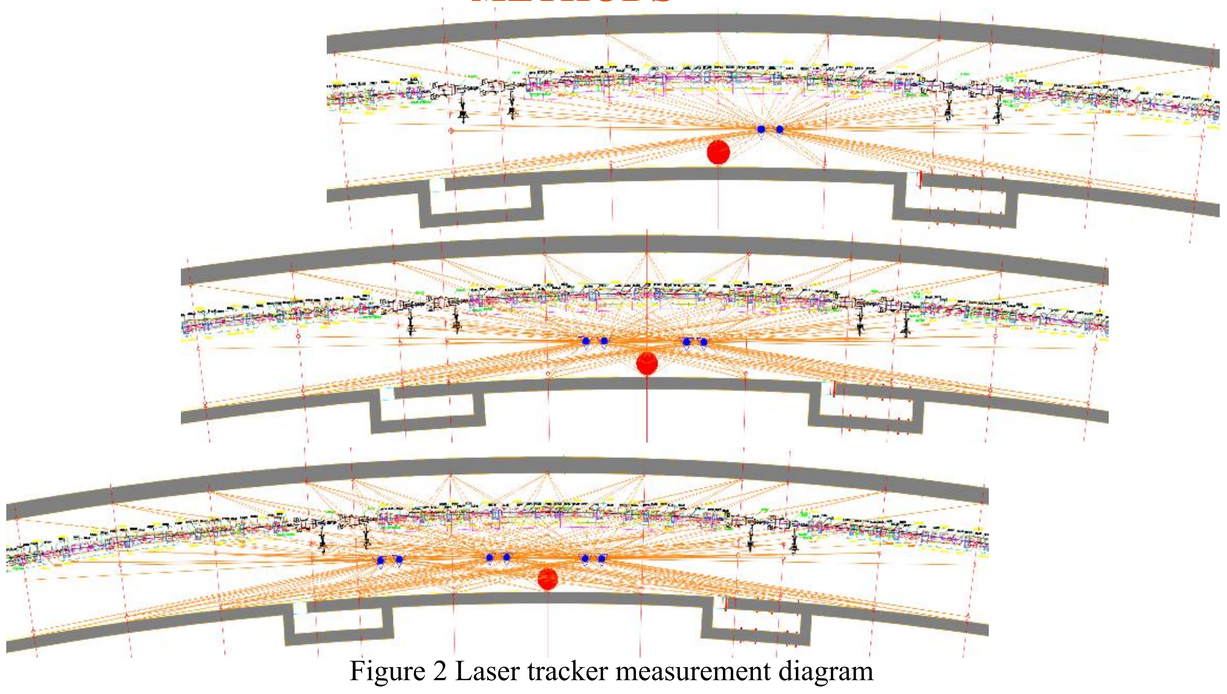

Figure 2 Laser tracker measurement diagram

The comprehensive measurement of the storage ring adopts a dual-instrument parallel comprehensive measurement scheme.

The double-sided measurement method with a laser tracker was adopted for observation, and the observation quantity at each point was doubled.

The observation conditions of the same station, time, weather and measurement points for two rounds of tunnel network measurements have been achieved, minimizing random errors to the greatest extent and significantly improving the repeatability of the two rounds of measurements.

The planar relative point position accuracy has reached 0.02mm, and the elevation is 0.084mm. The absolute accuracy of the plane has reached 0.2mm, with an elevation of 0.059mm, which is significantly improved compared to the point position accuracy of the third-generation light source and is on par with the point position accuracy of international tunnels.

RESULT

Table 1 Comprehensive measurement error after precise alignment

Comprehensive measurement error after precise alignment			
error statistics	MR/mm	MT/mm	MH/mm
two times measurement coordinates deviation	0.230	0.190	0.085
single-pass measurement error	**0.163** =0.230/$\sqrt{2}$	**0.134** =0.190/$\sqrt{2}$	**0.060** =0.085 /$\sqrt{2}$

Table 2 Absolute deviation of storage ring devices from theoretical positions

The deviation between the actual position and the theoretical position of the storage ring magnet（only unit points）			
deviation statistics	MR/mm	MT/mm	MH/mm
maximum deviation	0.197	0.300	0.178
Minimum deviation	-0.305	-0.163	-0.129
RMS	**0.136**	**0.056**	**0.061**
mean deviation	-0.058	-0.001	-0.004

The displacement method was adopted to precisely and directly adjust the theoretical position of the storage ring.

After the absolute position alignment, a comprehensive measurement was conducted again using two instruments in parallel. The coordinate deviations in the radial, tangential, and vertical directions and the standard deviation of the single measurement are shown in Table 1.

The comprehensive measurement results after the absolute position alignment show that the maximum deviation of the absolute position of the magnet is 0.305 mm and the standard deviation of the absolute position is 0.136 mm, from table 2.

The subsequent test indicators of the high energy photon source all meet or exceed the approved acceptance indicators, and the precise and direct adjustment of the theoretical position of the storage ring meets the accuracy requirements.

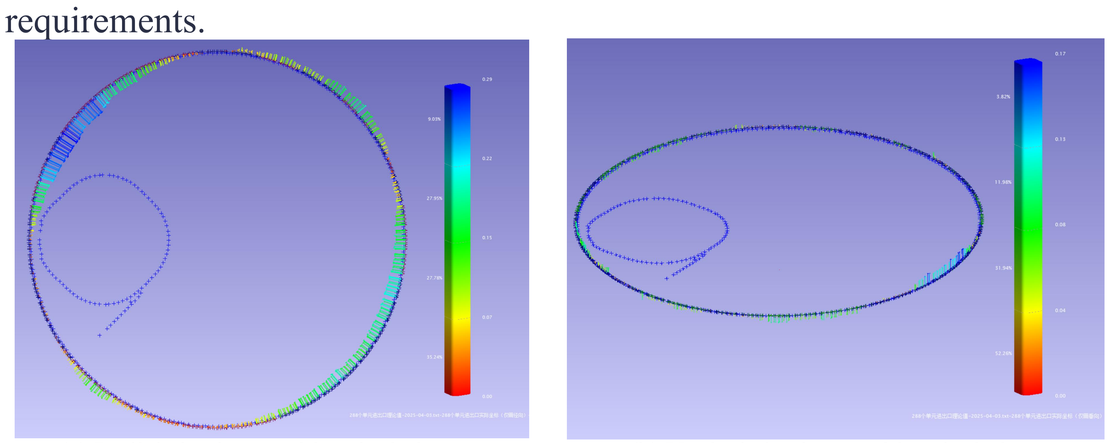

(a) Radial absolute position deviation (b) Vertical absolute position deviation

Figure 3 Absolute position deviation of unit magnets after absolute position alignment of the storage ring

† email address: yanhy@ihep.ac.cn dongl@ihep.ac.cn wxl@ihep.ac.cn

A07

Development of a hybrid superconducting dipole magnet with the magnetic field beyond 14 T

中国科学院高能物理研究所
Institute of High Energy Physics
Chinese Academy of Sciences

Chengtao Wang*, Junqing Wang, Ze Feng, Wei Li, Huang Yang, Yingzhe Wang, Rui Ma, Hang Xu, Qingyuan Li, Fan Ren, Qi Zhang, Menglin Wang, Chunyan Li, Juan Wang, Rui Kang, Jin Zhou, Xin Chen and Qingjin Xu*

IHEP, CAS (Institute of High Energy Physics, Chinese Academy of Sciences)

中科院高能所超导磁体组
Superconducting Magnet Group, IHEP

High field dipole magnets R&D steps

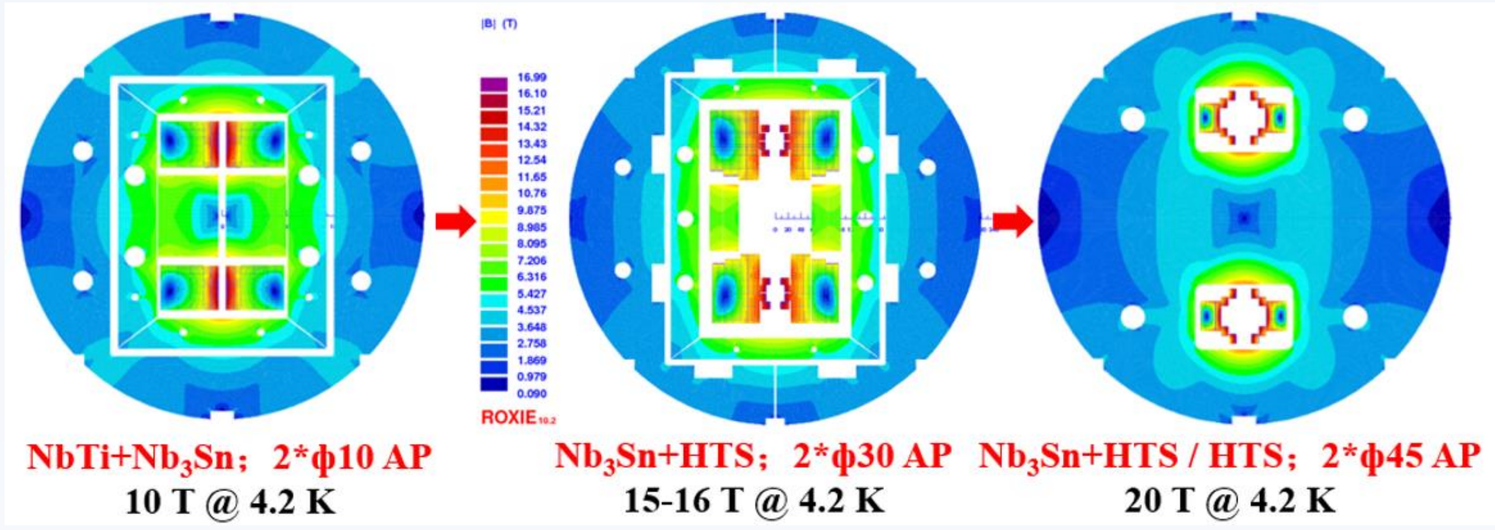

Specification:

The fabrication of high field dipole magnets				
R&D steps	Magnet name	Aperture diameter	Main field	Status
Step 1	LPF1	10 mm	10.23 T	Completed
	LPF1-S	12 mm	10.71 T	Completed
	LPF1-U	14 mm	12.47 T	Completed
Step 2	LPF3-U	~20 mm	14.5 T	Completed
	LPF3-U1	~30 mm	To be 16 T	On going
Step 3	LPF4…	~50 mm	Beyond 16 T	Next

Design of the hybrid dipole magnet - LPF3-U (LTS-10 T + HTS-6 T)

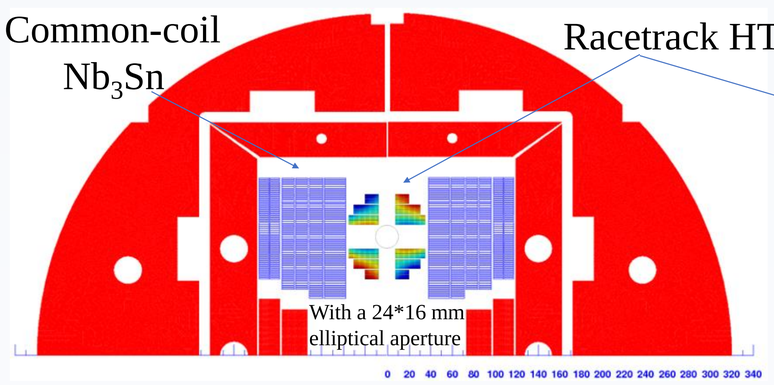

The cross-section of LPF3-U

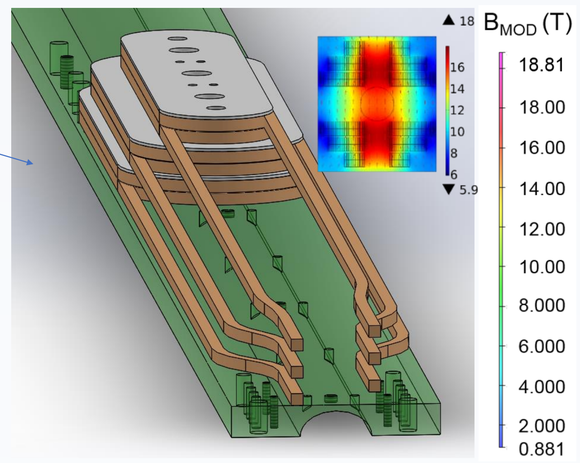

HTS insert coil design

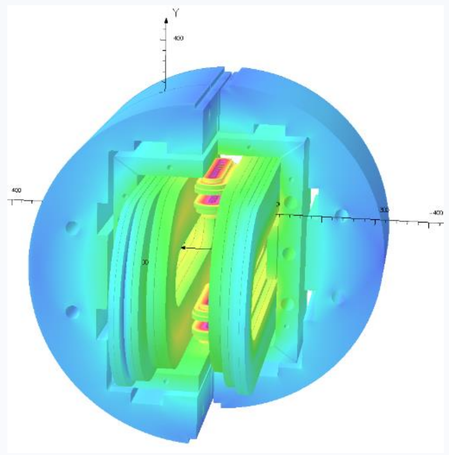

Field distribution in the LPF3-U

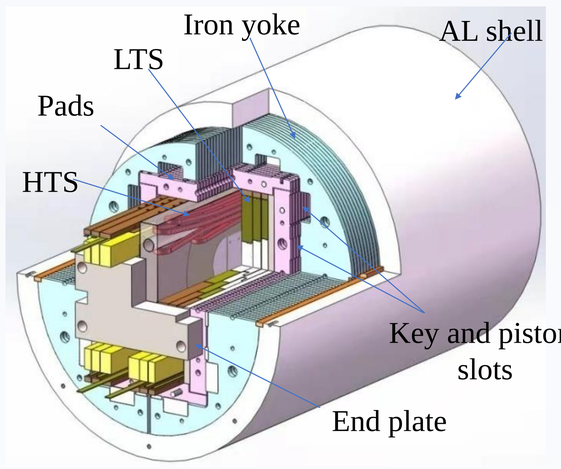

Schematic diagram of LPF3-U

Fabrication and performance tests of LPF3-U dipole magnet

LPF3-U dipole magnet

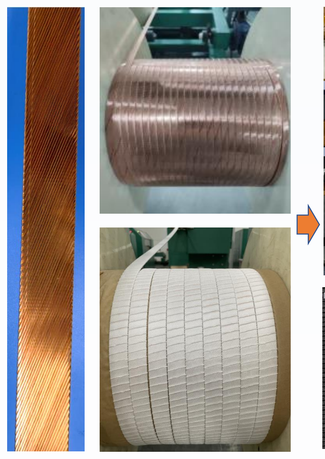

Rutherford cable R&D

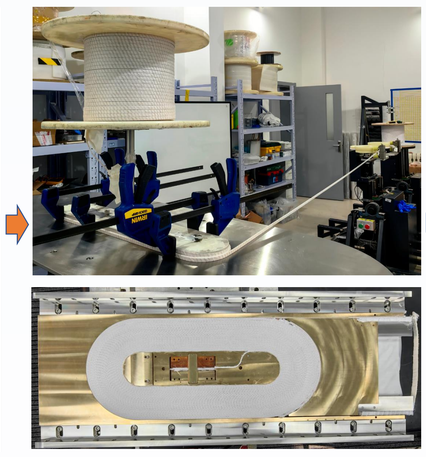

Nb_3Sn coil winding

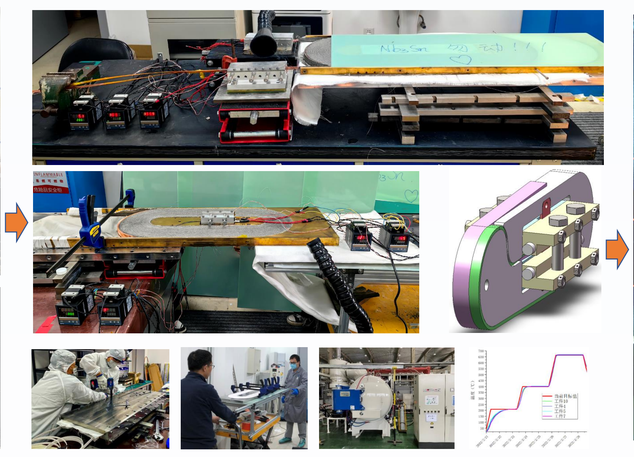

Splices R&D

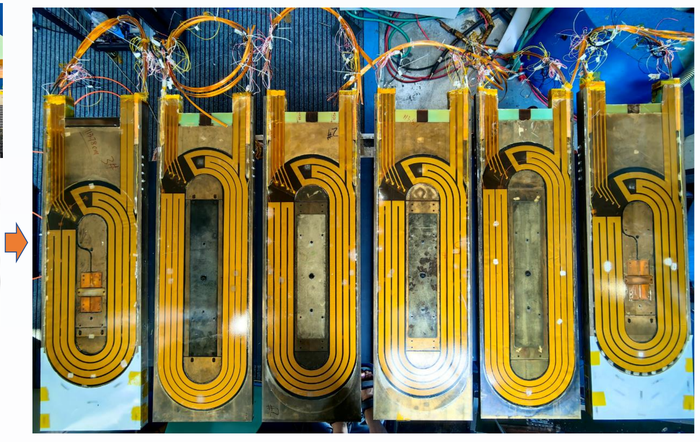

Nb_3Sn coils after VPI

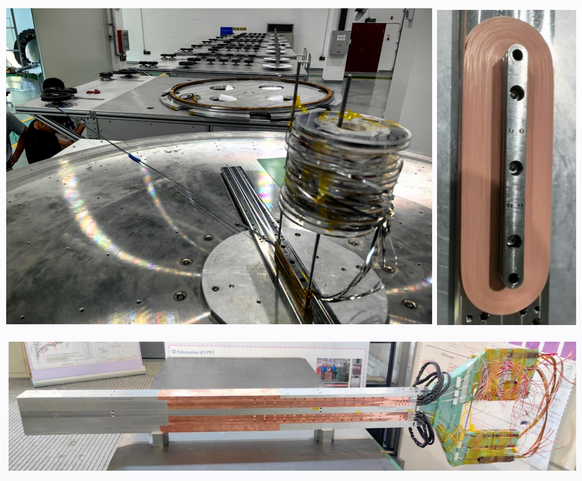

Fabrication of HTS insert coil

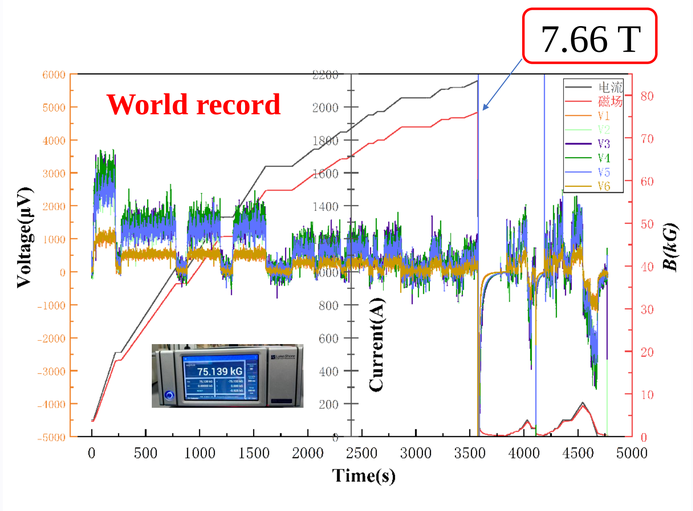

Performance of HTS insert coil

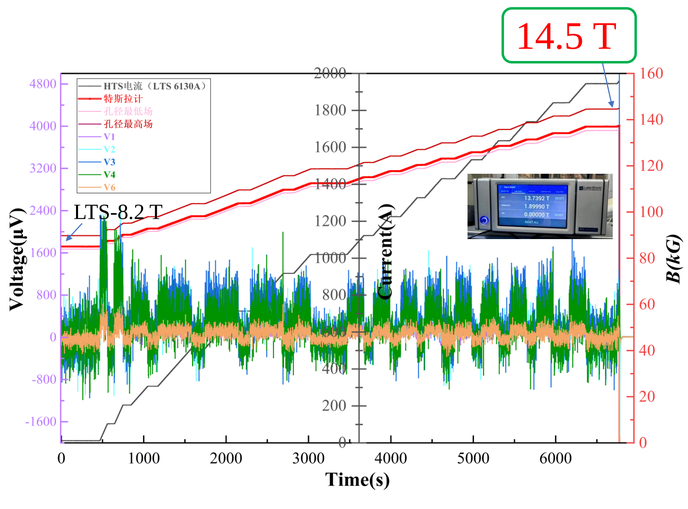

Performance of LPF3-U magnet

A series of subscale dipole magnets featuring hybrid NbTi, Nb_3Sn, and REBCO superconducting coils have been developed at IHEP, with progressively enhanced design complexity and electromagnetic performance. The most recent prototype, LPF3-U, achieved a peak field of 14.5 T within a 24×16 mm aperture. Currently, an upgraded magnet, LPF3-U1, is under assembly, with performance testing scheduled for December 2025. This enhanced prototype is anticipated to demonstrate further improvement in the central magnetic field strength.

Email: wangct@ihep.ac.cn; xuqj@ihep.ac.cn

Closed-loop ReBCO Coil Under Varying Magentic Field: A Study of its Current Distribution and Dynamic Losses

A08

Hang Xu[1, 2], Rui Kang[2], Rui Ma[1, 2], Juan Wang[2], Qingjin Xu*[2]

(1. University of Chinese Academy of Sciences, Beijing 100049; 2. Institute of High Energy Physics, Beijing 100049)

中国科学院高能物理研究所
Institute of High Energy Physics, IHEP

Abstract

In this work, a 2D axisymmetric model was established based on the H-formulation.By coupling electromagnetic and thermal modules, the variation in dynamic losses of the NI closed-loop HTS coil was analyzed when an induced current was generated under a parallel time-varying external magnetic field. The accuracy of the simulation calculations was verified by measuring the coil's temperature rise. Furthermore, the research was extended to the combined structure of insulated (INS) and non-insulated (NI) HTS coils: for this combined structure, the current density distribution and dynamic loss variation of the coil were analyzed, and the dynamic loss characteristics of the coil under complex electromagnetic fields were discussed in detail. This study provides a theoretical basis and technical reference for optimizing the design of HTS coils and reducing their dynamic losses.

Modelling method

Modeling of non-insulated coils:

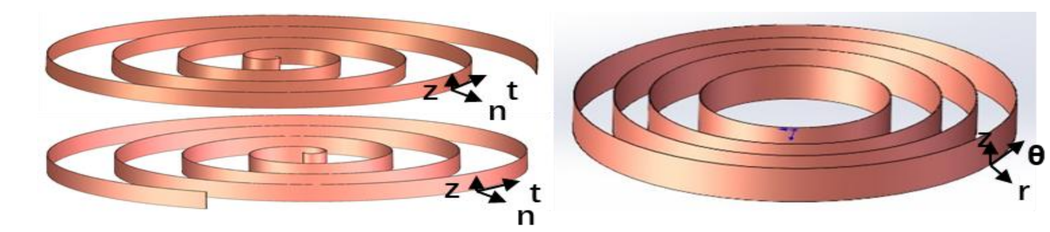

$$g = \begin{pmatrix} \cos\alpha & -sin\alpha \\ sin\alpha & cos\alpha \end{pmatrix} \text{ (anticlockwise)} \qquad \begin{pmatrix} n \\ t \end{pmatrix} = g \cdot \begin{pmatrix} r \\ \varphi \end{pmatrix}$$

$$g = \begin{pmatrix} \cos\alpha & sin\alpha \\ sin\alpha & -cos\alpha \end{pmatrix} \text{ (clockwise)}$$

$$J_r = -\frac{\partial H_\varphi}{\partial z} \qquad E_r = \rho_{rr}J_r + \rho_{r\varphi}J_\varphi \qquad \mu\frac{\partial H_r}{\partial t} + \left(-\frac{\partial E_\varphi}{\partial z}\right) = 0$$

$$J_\varphi = \frac{\partial H_r}{\partial z} - \frac{\partial H_z}{\partial r} \Rightarrow E_\varphi = \rho_{\varphi r}J_r + \rho_{\varphi\varphi}J_\varphi \Rightarrow \mu\frac{\partial H_\varphi}{\partial t} + \left(\frac{\partial E_r}{\partial z} - \frac{\partial E_z}{\partial r}\right) = 0$$

$$J_z = \frac{1}{r}\frac{\partial (rH_\varphi)}{\partial r} \qquad E_z = \rho_z J_z \qquad \mu\frac{\partial H_z}{\partial t} + \left(\frac{1}{r}\frac{\partial (rE_\varphi)}{\partial r}\right) = 0$$

resistivity: $\rho_{sc} = \frac{E_C}{J_C(B,T)}\left|\frac{J}{J_C(B,T)}\right|^{(n-1)}$

dynamic loss: $Q = Q_n + Q_t$

coupling loss: $Q_n = \iiint \rho_n J_n^2 dv$ hysteresis loss: $Q_t = \iiint \rho_t J_t^2 dv$

Parameters of HTS coils

Parameters	Value(100mm)	Value(1m)
HTS tape's width(mm)	4	5
HTS tape's thickness(mm)	0.1	0.1
HTS coil's radius(mm)	50	500
I_{c0}@77K(A)	200	200
n	20	20
μ_0(H/m)	$4\pi*10^{-7}$	$4\pi*10^{-7}$
α_0	1.5181	1.5181
β	2.3251	2.3251
Inter-turn resistivity(Ω·m²)	10^{-11}	-

Model of HTS coils

rotating coil:
- Non-insulation
- Simplified modeling

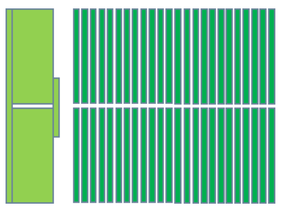

Background coil:
- Insulation
- Independent modeling

Dynamic loss of 100mm coils

Numerical model:

- Only consider the superconducting layer

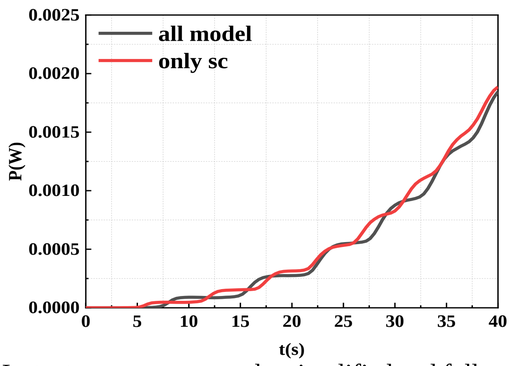

Instantaneous power under simplified and full models

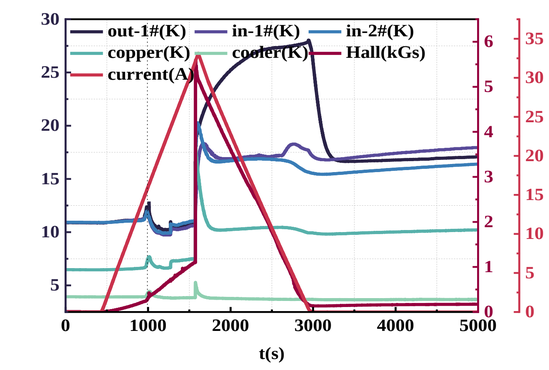

Temperature and shielding magnetic field changes

Experiment:

- Thermal method

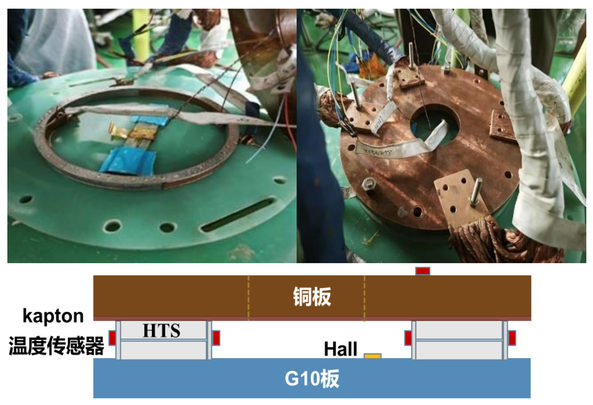

Dynamic loss experiment of rotating coil excitation

- The calculation error of the simplified model is less than 5%
- Rotating coils will generate dynamic losses under changing external fields
- Dynamic loss causes the coil temperature to rise

Dynamic loss of 1m coils

Excitation rate:

- The greater the excitation rate, the greater the instantaneous power

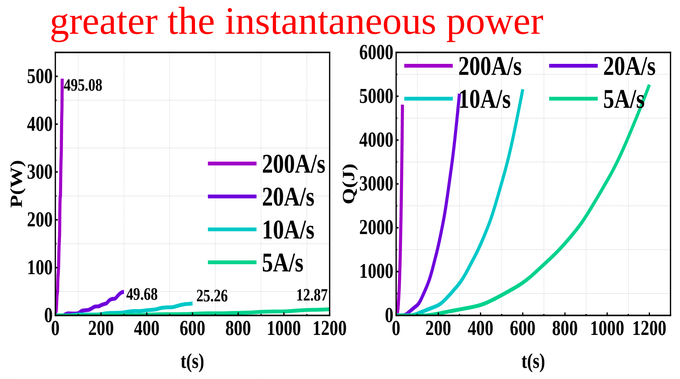

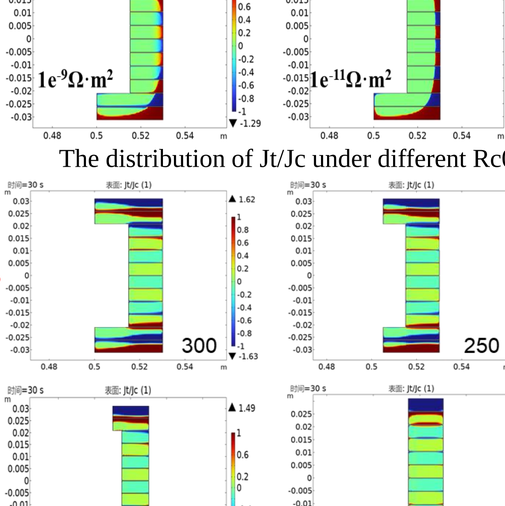

Dynamic losses of different Jt/Jc at different excitation rates

Inter-turn resistivity:

- The smaller the inter-turn resistivity, the greater the dynamic loss

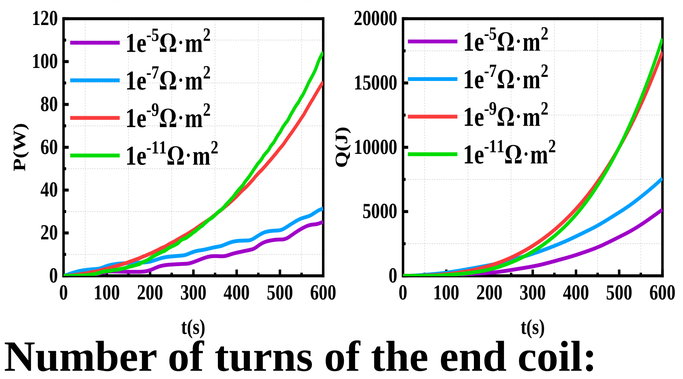

The distribution of Jt/Jc under different Rc0

Number of turns of the end coil:

- The number of turns in the end coil has the greatest impact on dynamic loss

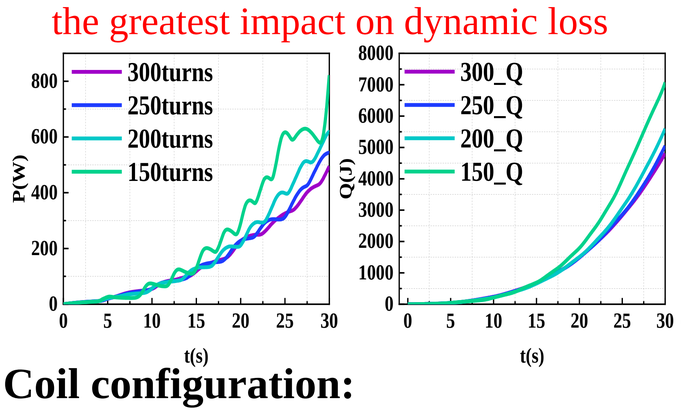

The distribution of Jt/Jc under different turns

Coil configuration:

- Series connection of coils can reduce dynamic losses

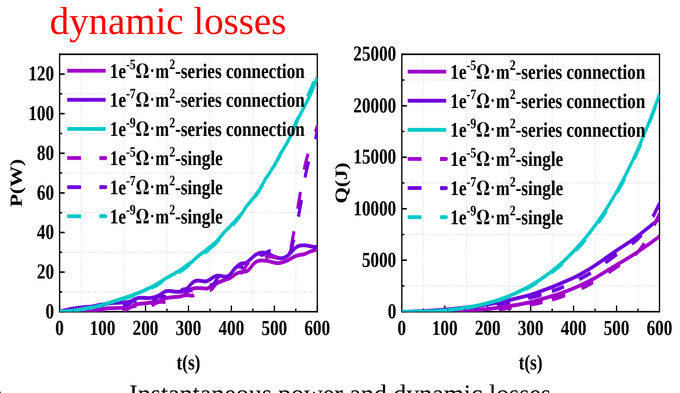

Instantaneous power and dynamic losses

The distribution of Jt/Jc under different connection methods

A09

Development of a CLIQ-Varistor Quench Protection Scheme for the LPF3-U Superconducting Dipole Magnet

Junqing Wang[1,2] ， Ze Feng[1,2]， Rui Kang[2]， Jin Zhou[2] ， Xin Chen[2]， Chengtao Wang[1,2,*] ， Qingjin Xu[1,2, *]

（1. University of Chinese Academy of Sciences； 2. Institute of High Energy Physics, CAS）

INTRODUCTION

For the pre-study of the Super Proton-Proton Collider (SPPC) project, the Institute of High Energy Physics (IHEP) has developed the LPF3-U, designed to achieve a 16 T dipole field within a 16*24 mm^2 aperture.

The LPF3-U magnet integrates six Nb_3Sn coils in a Common-Coil configuration, accompanied by an HTS insert that utilizes seven YBCO tapes wound in parallel with a stainless-steel tape in a racetrack coil structure.

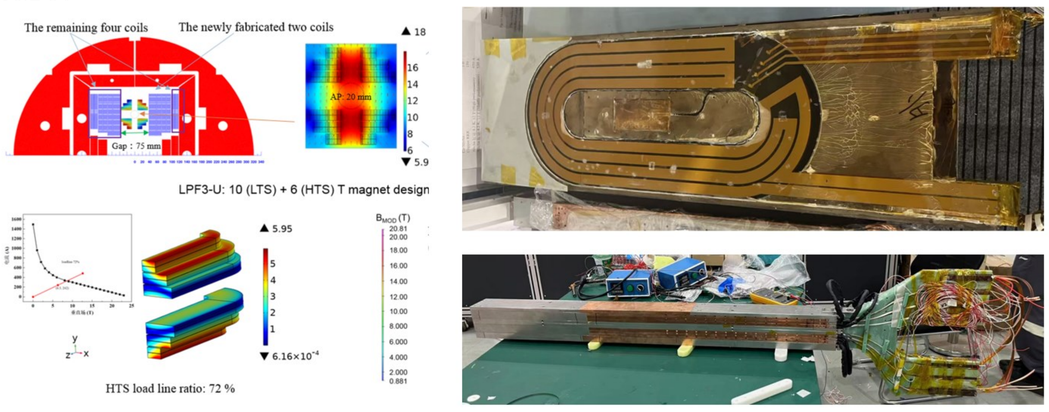

Fig.1. Electromagnetic Design and Physical Diagram of LPF3-U

LTS magnet stores 2.1 MJ at 7580 A, HTS insert magnet 0.166 MJ at 2180 A, and mutual inductance energy between them is 0.04 MJ.

CLIQ Quench Protection Scheme For the LPF3-U

Through calculations, the segmenting scheme that minimizes the equivalent inductance of the circuit is 1, 3, 2, 5-4, 6.

• Circuit Model and the Optimal CLIQ Scheme

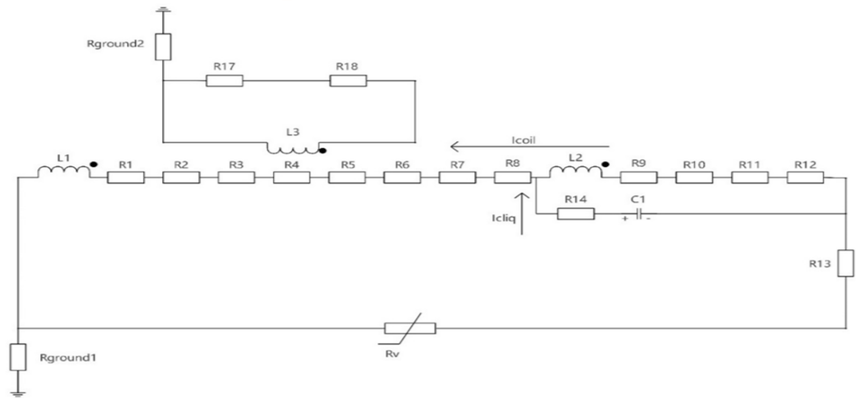

Fig.2. Quench Protection Circuit Model of LTS Magnet

In hybrid magnets, the mutual inductance coupling between magnets must be considered when analyzing the performance of CLIQ.

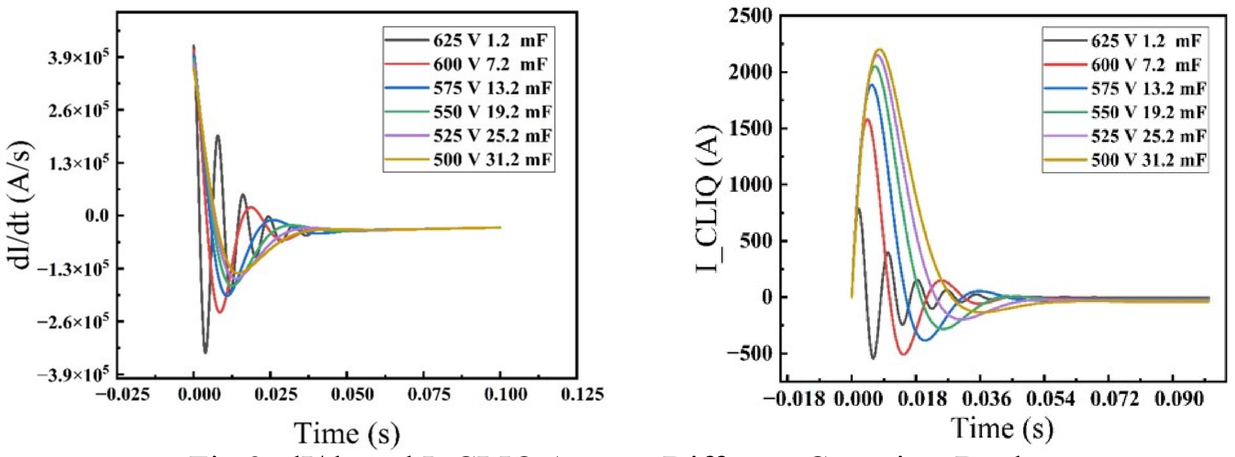

Fig.3. dI/dt and I_CLIQ Among Different Capacitor Banks

By comparing results such as CLIQ efficiency, action time, and heat transfer calculations, 7.2 mF@600 V is selected as the optimal CLIQ scheme

• Simulation Results and Experiment

Calculations indicate that the maximum voltage to ground is 918 V and the maximum hot-spot temperature is 318 K, both within the safe range. To date, 30 safe LTS quench protections have been achieved in the tests of three generations of LPF3-U magnets.

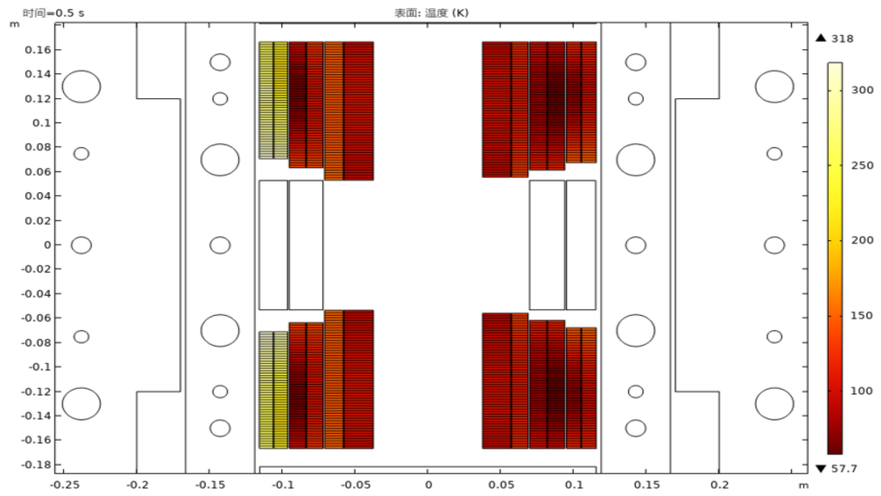

Fig.4. Temperature Distribution of Quenched Coils in LTS at 7580 A

Quench Damage Analysis and Self-Protection Scheme of HTS

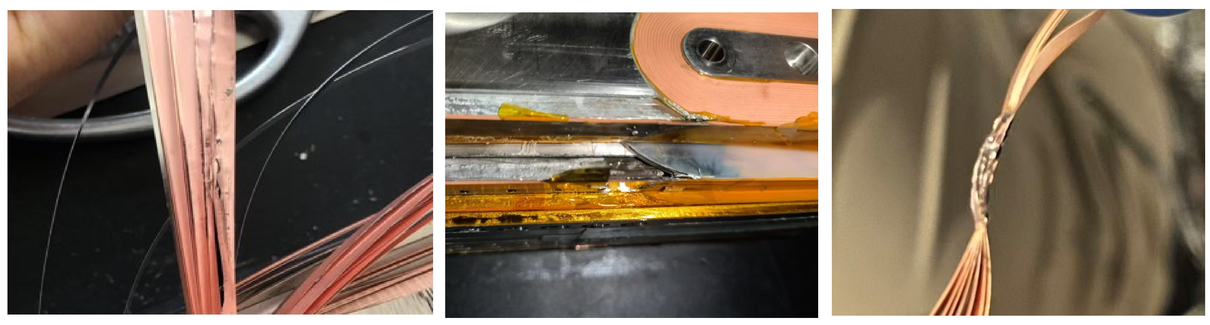

Fig.5. Typical damage Types of NI/MI HTS coils

When the HTS insert magnet is subjected to the quench of the background magnet or its own high-current quench, there is a high risk of damages such as REBCO tape mechanical damage, voltage breakdown, and overheating burnout. NI/MI coils allow significant intra-turn and inter-turn shunting, which greatly improves the self-protection performance of the magnet; however, the extremely small inter-turn resistance also prevents effective energy release outside the magnet.

The shielding measure reduces the induced current from over 2000 A to 1300 A

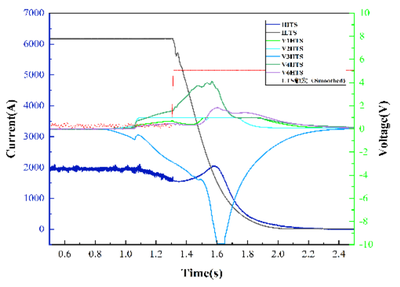

The insulation design, together with additional parallel superconducting strips

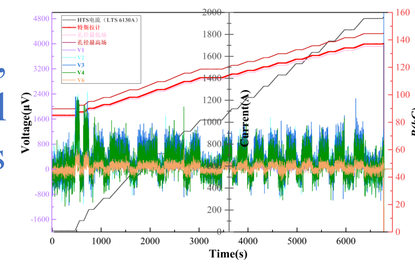

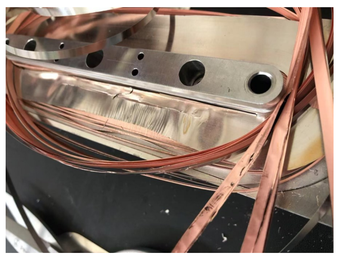

Adjust the winding tension and assembly preload, and add mechanical buffers at key positions

In addition, the design and optimization of the HTS self-protection scheme have been carried out through solutions such as thermal conductivity design, joint technology, inter-turn resistance optimization, and the balance between loadline and copper plating thickness. Furthermore, a scientific hybrid magnet excitation scheme can also avoid HTS quench damage to a great extent.

Optimized self-protection design enables the HTS insert magnet to reach a 7.66 T bore center field at 2159 A, and assists the LPF3-U magnet in achieving 13.74 T (bore center) and 14.49 T (maximum bore) via combined excitation.

中国科学院大学 University of Chinese Academy of Sciences

中国科学院高能物理研究所 Institute of High Energy Physics, Chinese Academy of Sciences

A10

Simulation and Experimental Validation of Inductive Excitation in HTS Flywheel Energy Storage System

Rui Ma [1,2], Juan Wang [1], Jin Zhou [1], Kai Liao [1,2], Hang Xu [1,2], Rui Kang[1]*, Qingjin Xu[1]*

1. Institute of High Energy Physics, Chinese Academy of Sciences
2. University of Chinese Academy of Sciences

A-10

Abstract

- Traditional flywheel energy storage technology is limited by the mechanical strength of materials, resulting in a theoretical upper limit on flywheel rotational speed. To address this bottleneck, IHEP has proposed a new ring-shaped superconducting kinetic energy loading system. This system provides centripetal force through radial electromagnetic force, breaking the speed limitation. An external back-field solenoid coil supplies the magnetic field to the internal flywheel coil, and the flywheel coil is energized through **induction excitation**. This method of inductive energization effectively reduces the impedance issues caused by current leads under rotational conditions. The flywheel coil is a **closed-loop**, **double-pancake wound**, **insulation-free coil**, **solidified with solder**, offering both a stable mechanical structure and excellent post-excitation current retention capability.

Coil Design

- To **minimize the time delay** when powering the back-field, high-temperature superconducting tape wrapped with Kapton is used for winding, and **Kapton** is used to provide **inter-turn insulation**.

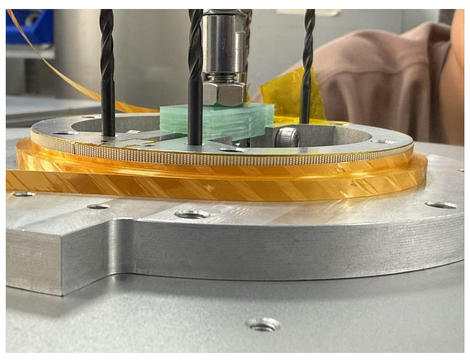
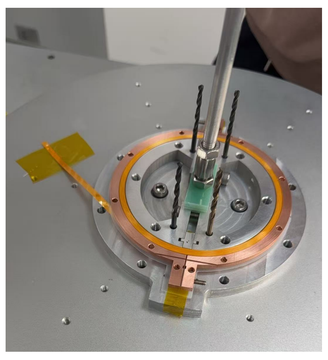
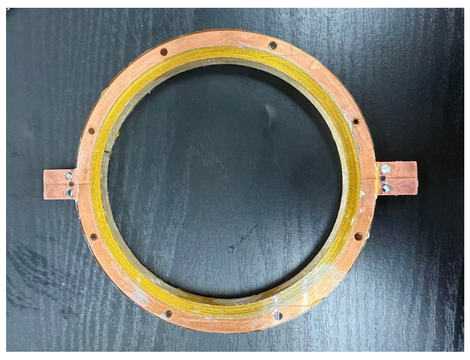

- The rotating coil is wound with copper-plated tape as **an uninsulated double pancake**. On the outermost layer, 4mm strips are used to weld the double pancake coils together in a manner opposite to the superconducting layer, **forming a closed loop**.

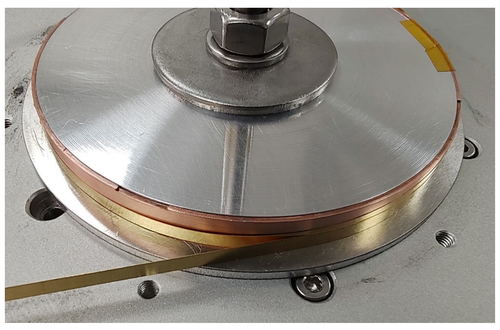
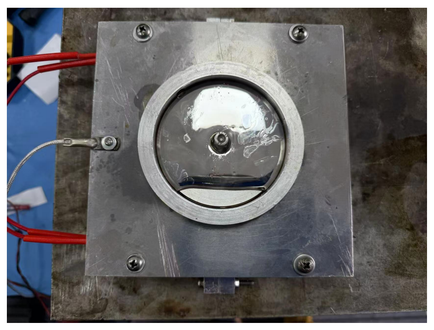


Experimental Measurement

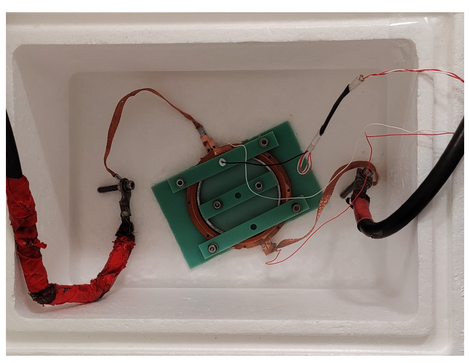

- Indirect measurement of induced current at 77K

Parameter	Unit	Value
Back-field coil inner/outer diameter	mm	56/61
Rotating coil inner/outer diameter	mm	50/54
Back-field coil current	A	40
Tape	--	Copper-plated
Critical current	A	>200A

Simulation Analysis

- Three sets of data were collected on the data acquisition instrument: the back-field coil end voltage signal, the back-field coil current signal, and the Hall probe signal.
- The Hall probe signal is used to indirectly measure the induced current on the rotating coil.

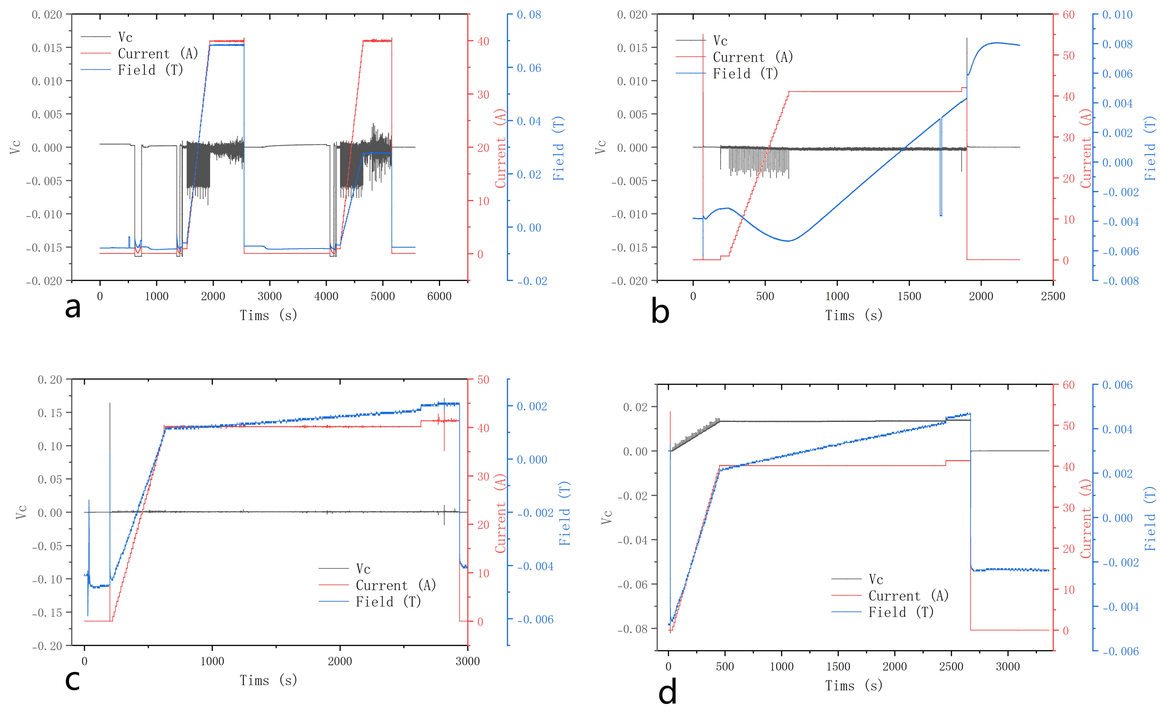

- Figure a: Magnetic field data measured from a **single background coil**. The magnetic field is completely **linearly related to the current**.
- Figure b: Magnetic field changes at the **edge aperture** during three stages: power-on, constant current, and power-off
- Figures c and d: Magnetic field changes at the **central aperture** during three stages: power-on, constant current, and power-off

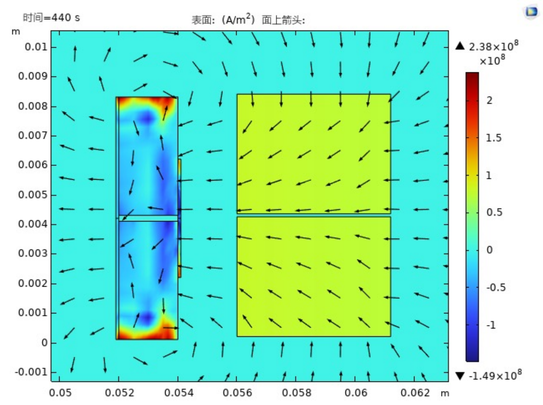

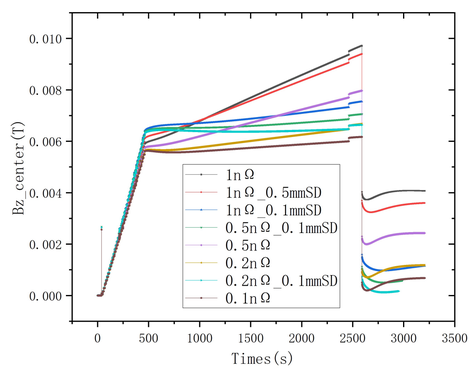

- In the comparison between simulation and experimental results, the main adjustments are made to the two parameters: **inter-turn resistance** and **joint resistance**.
- In the comparison between experimental data and COMSOL simulation data, the trends are basically consistent, and the **joint resistance** of the coil without insulation after solder solidification is controlled **below 1 nΩ**.

Conclusion

- This experiment, combining electromagnetic simulation with experimental verification, confirmed **the feasibility of the induction excitation method** along with solder curing closed-loop and **the continuous current-carrying capability** of the double pancake coil, laying an important foundation for the innovative design of a new ring-shaped superconducting kinetic energy loading system.

CEPC 2025

A11

1. 中国科学院高能物理研究所 Institute of High Energy Physics, CAS
2. 北京工业大学 Beijing University of Technology
3. 中国科学院电工研究所 Institute of Electrical Engineering, CAS
4. 中国科学院等离子体物理研究所 Institute of Plasma Physics, CAS

Electromagnetic Properties of Iron-Based Superconducting Uninsulated Double Pancake Coils and Their Comparison with REBCO Coils

Fan Ren[1,2], Chunyan Li[1], Yanchang Zhu[3], Jin Zhou[1], Xianping Zhang[3], Min Liu[2], Fang Liu[4], Yanwei Ma[3] and Qingjin Xu[1]

(1. Institute of High Energy Physics, Chinese Academy of Sciences, Beijing 100049; 2. Key Laboratory of Advanced Functional Materials, Beijing University of Technology, Beijing 100124; 3. Institute of Electrical Engineering, Beijing 100190; 4. Institute of Plasma Physics, Hefei 230031)

Abstract

➢ Iron-based superconductors show great potential for high-field magnet applications. The electromagnetic properties of iron-based superconducting (IBS) uninsulated coils are crucial for their future practical applications, yet characteristics such as charging delay and turn-to-turn contact resistivity (R_{ct}) remain poorly understood. To address this, we fabricated metal-insulation (MI) and no-insulation (NI) iron-based superconducting double pancake coils (DPCs) and systematically tested their charging and sudden-discharging behaviors. Experimental results revealed that the R_{ct} of the IBS-MI coil is 6.3 times higher than that of the IBS-NI coil, along with a significantly shorter charging delay. Moreover, an interesting phenomenon was discovered: the R_{ct} of uninsulated IBS coils is much lower than that of the REBCO coils reported in previous studies. For rigorous verification of this finding, MI and NI REBCO coils were prepared and subjected to charging and sudden-discharging tests. Through comparison, it is found that the R_{ct} of the REBCO-MI coil is 73.6 times greater than that of the IBS-MI coil, while the R_{ct} of the REBCO-NI coil is 3.6 times greater than that of the IBS-NI coil. The main reasons for this difference will also be analyzed in this paper. From an application perspective, the low R_{ct} of uninsulated coils also means high thermal stability and self-protection. This work lays the foundation for investigating the proportional and integral (PI) feedback control method to eliminate magnetic field delays and for validating the thermal stability of IBS uninsulated coils in future studies.

Experimental Methods

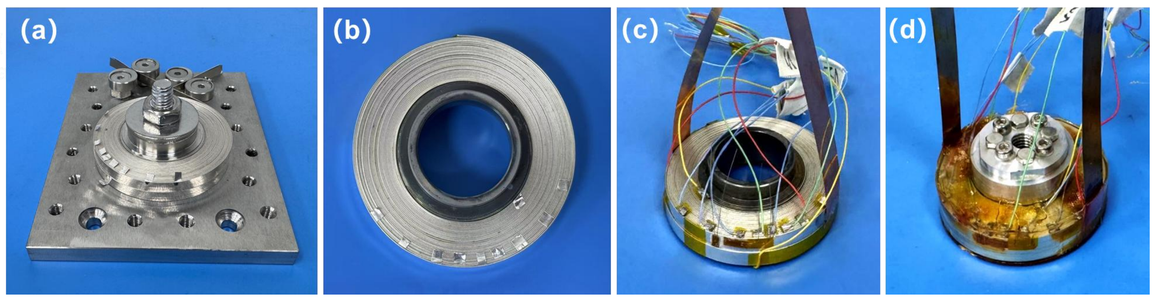

Figure 1. Detailed photographs taken during the fabrication process of IBS double pancake coils. (a) IBS-MI coil fixing. (b) IBS-MI coil after heat treatment. (c) IBS-MI coil after completing the joint and voltage leads soldering. (d) IBS-MI coil after epoxy impregnation.

✓ The IBS-MI and IBS-NI coils were wound using AgSn/Ag-sheathed Ba122 tapes under a tension of 50 N. During the winding process, the IBS-MI coil was co-wound with a 0.05 mm thick stainless steel (SS) tape. After winding, both coils underwent a heat treatment at 880 °C for 1 hour, followed by epoxy resin impregnation for curing.

Figure 2. Photogaph of the REBCO-MI coil.

✓ REBCO-MI, REBCO-NI, and REBCO-NI+IPI coil were wound using 4 mm wide REBCO tape under a constant tension of 50 N.

✓ REBCO-NI coil was wound solely with superconducting tape.

✓ REBCO-MI coil was co-wound with superconducting tape and SS tape.

✓ REBCO-NI+IPI coil was incorporated with 0.15 mm thick Kapton as inter-pancake insulation between double-pancake windings.

Table 1. Parameters of the coils.

Coil parameter	Unit	IBS-MI	IBS-NI	REBCO-MI	REBCO-NI	REBCO-NI+IPI
Inner diameter	mm	33	33	33	33	33
Outer diameter	mm	53.2	53.5	41	38.9	38.9
Winding tension	N	50	50	50	50	50
Number of turns (N)	--	28	33	28	33	33
Number of layers	--	2	2	2	2	2
Superconducting tape width	mm	4.7	4.7	4	4	4
Superconducting tape thickness	mm	0.31	0.31	0.09	0.09	0.09
I_c @4.2K/10T	A	135	135	750	750	750
Inter-pancake insulation	--	/	/	/	/	Kapton sheet
Width of co-wound SS tape	mm	5	/	5	/	/
Thickness of co-wound SS tape	mm	0.05	/	0.05	/	/
Coil inductance (L_{coil})	mH	0.1394	0.1978	0.1391	0.2034	0.2017
Coil constant (K)	mT·A^{-1}	1.57	1.81	1.7	2.2	2.2

➢ Charging and sudden-discharging tests were conducted under the conditions of 4.2 K and 10 T.

➢ The direction of the background magnetic field was parallel to the width direction of the superconducting tape inside the coil.

Results and Discussion

➢ The coil was charged to 50 A at three current ramping rates (0.1, 1, and 10 A/s) and held at this current for a certain period; after the magnetic field stabilized, the power supply was cut off.

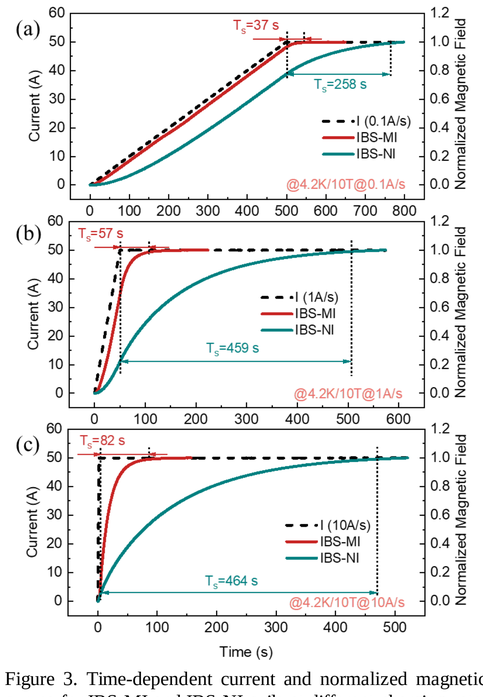

Figure 3. Time-dependent current and normalized magnetic field curves for IBS-MI and IBS-NI coils at different charging rates.

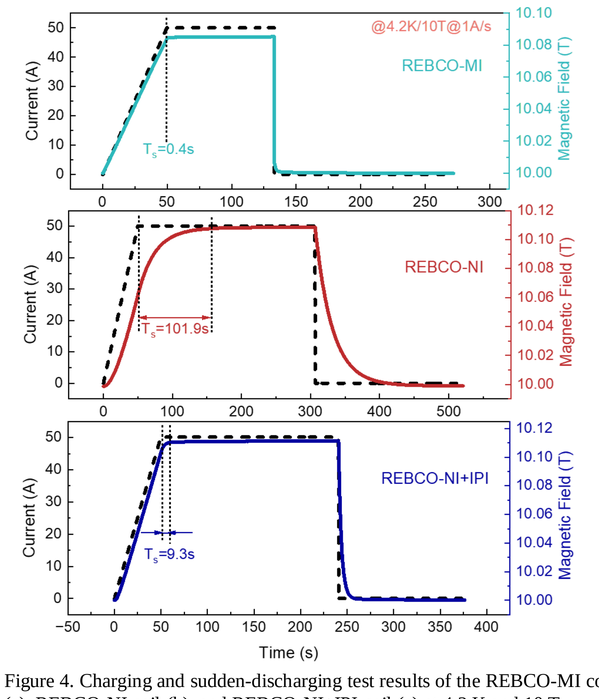

Figure 4. Charging and sudden-discharging test results of the REBCO-MI coil (a), REBCO-NI coil (b), and REBCO-NI+IPI coil (c) at 4.2 K and 10 T.

✓ At the same charging rate, the T_s of the IBS-MI coil is always significantly shorter than that of the IBS-NI coil.

Table 2. Key electromagnetic parameters of coils.

Coil	τ (s)	R_c (μΩ)	R_{ct} (μΩ·cm^2)
IBS-MI	16.3	8.55	1.017
IBS-NI	123.1	1.60	0.160
REBCO-MI	0.16	869.37	74.856
REBCO-NI	25.0	8.14	0.574
REBCO-NI+IPI	3.16	63.79	4.503

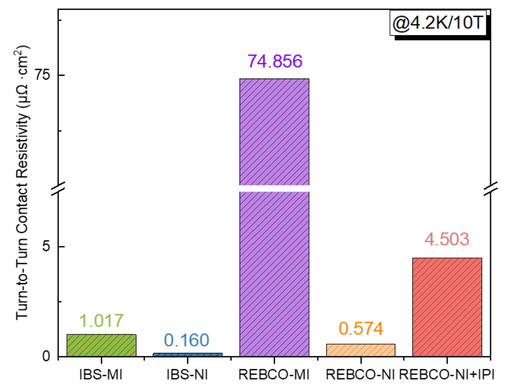

Figure 5. Comparison of R_{ct} between IBS and REBCO coils under MI and NI winding methods.

✓ The R_{ct} of the REBCO-NI+IPI coil is 4.503 $\mu\Omega\cdot cm^2$, which is 7.8 times that of REBCO-NI. This demonstrates that the 0.15 mm-thick Kapton sheet effectively serves as the layer insulation by blocking the shunting path between the pancakes.

✓ The R_{ct} of the REBCO-MI coil is 73.6 times that of the IBS-MI coil, while the R_{ct} of the REBCO-NI coil is 3.6 times that of the IBS-NI coil.

Figure 6. Photograph of the cross-section of the IBS-NI coil after heat treatment.

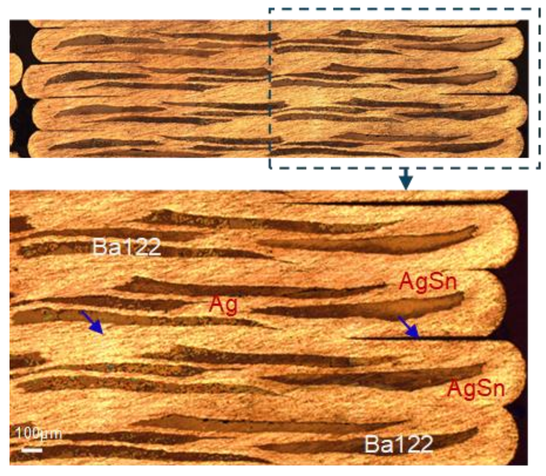

Figure 7. Cross-sectional morphology of the IBS-MI coil after heat treatment.

✓ Between adjacent IBS tapes, gaps are only visible near the edges, whereas the central regions appear effectively fused.

结论

✓ Electromagnetic properties of IBS coils are affected by winding method : the R_{ct} of the IBS-MI coil is 6.3 times that of the IBS-NI coil, with shorter charging delay.

✓ The R_{ct} of IBS coils is significantly lower than that of REBCO coils. The core reason is that adjacent turns of IBS coils form partial diffusion bonding after heat treatment at 880°C, which increases the effective contact area.

A Low-Level Radio Frequency (LLRF) Control System for Multiple Superconducting Cavities Based on MicroTCA.4*

Wenbin Gao[1,2], Nan Gan†[1,2], Zusheng Zhou[1,2], Jiyuan Zhai[1,2], Xinpeng Ma[1]

Institute of High Energy Physics, Chinese Academy of Sciences, Beijing 100049, China[1]

University of Chinese Academy of Sciences, Beijing 100049, China[2]

中国科学院高能物理研究所
Institute of High Energy Physics
Chinese Academy of Sciences

ABSTRACT

This poster presents a domestically developed LLRF control system for simultaneously driving six superconducting cavities with a single klystron. Based on a fully domestic MicroTCA.4 platform, the system employs vector-sum control, IQ sampling, and feedforward-feedback techniques. It ultimately achieves high-precision amplitude, phase, and frequency control for the six cavities, validating a key step for the CEPC project.

VECTOR-SUM CONTROL PRINCIPLE

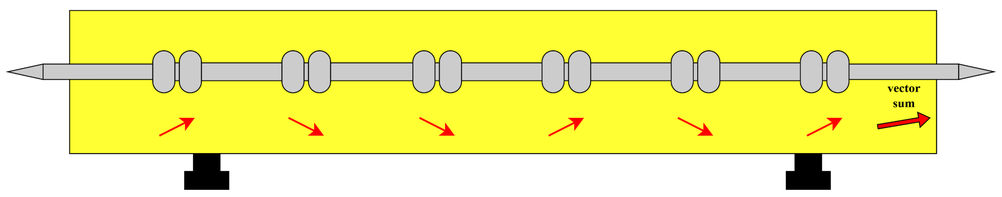

The Vector Sum Control Principle

$$\sum_{i=1}^{n} \vec{V}_{cavity\_i} = \vec{V}_{cavities\_sum}$$

OVERVIEW OF THE LLRF FOR MULTI-CAVITY

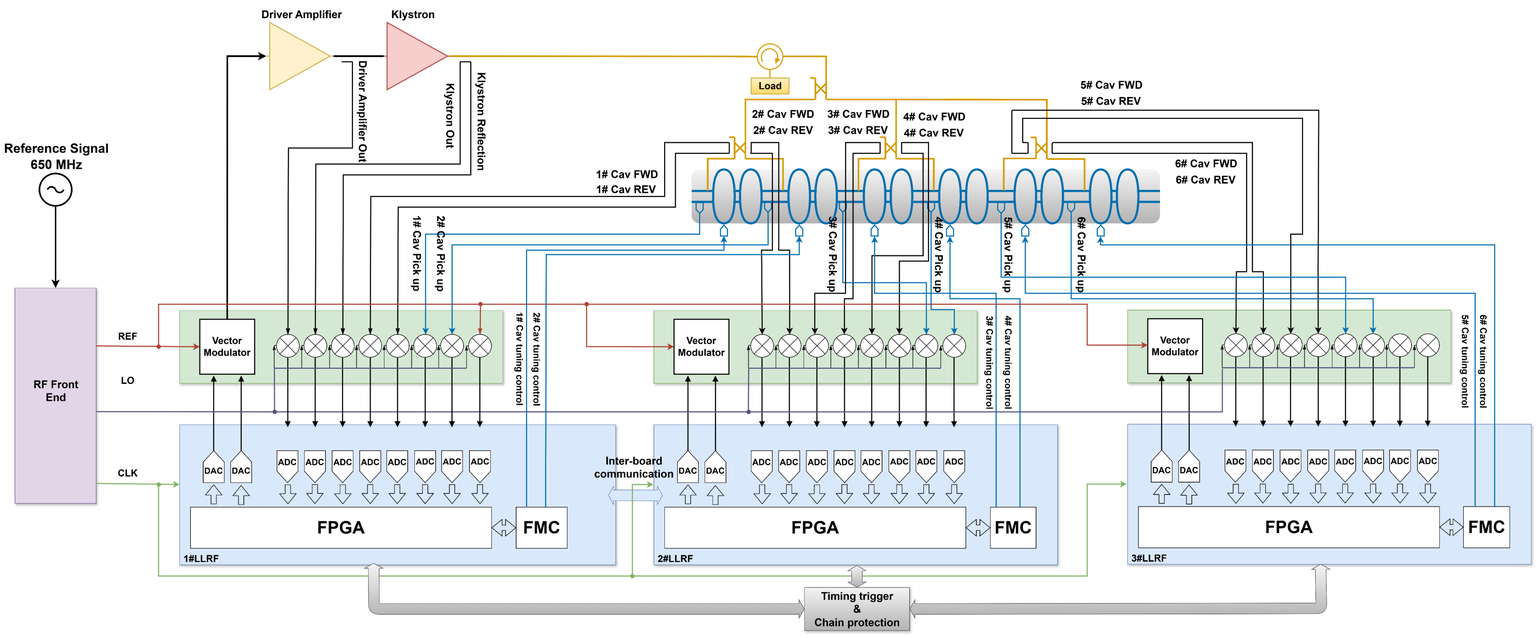

CEPC 650 MHz 6×2-cell superconducting module LLRF system design scheme

The system operates in a master-slave architecture, utilizing a unified vector-sum setpoint for global control, which eliminates per-cavity feedback loops to reduce cost and complexity. The tuning of individual cavities is achieved through a combination of feedforward and feedback control, ensuring precise adjustment.

FIRMWARE OF THE LLRF

Each of the three board cards handles the complete processing for two cavities, including signal demodulation, local vector summation, tuning, and quench detection. These local vector sums are then sent to the main board, which consolidates them into a global vector sum and generates the final feedback signals.

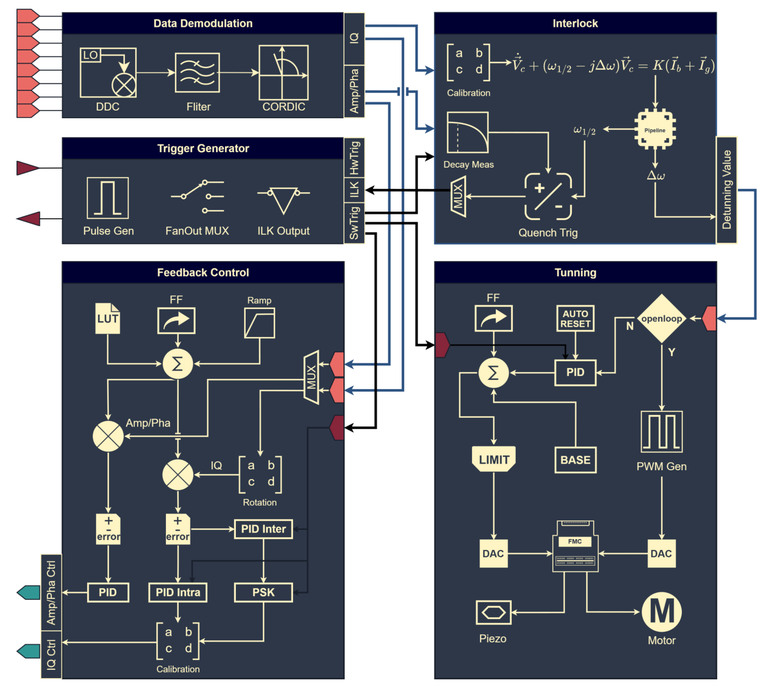

Firmware Architecture Diagram

DETUNING-CALCULATION FIRMWARE VERIFICATION

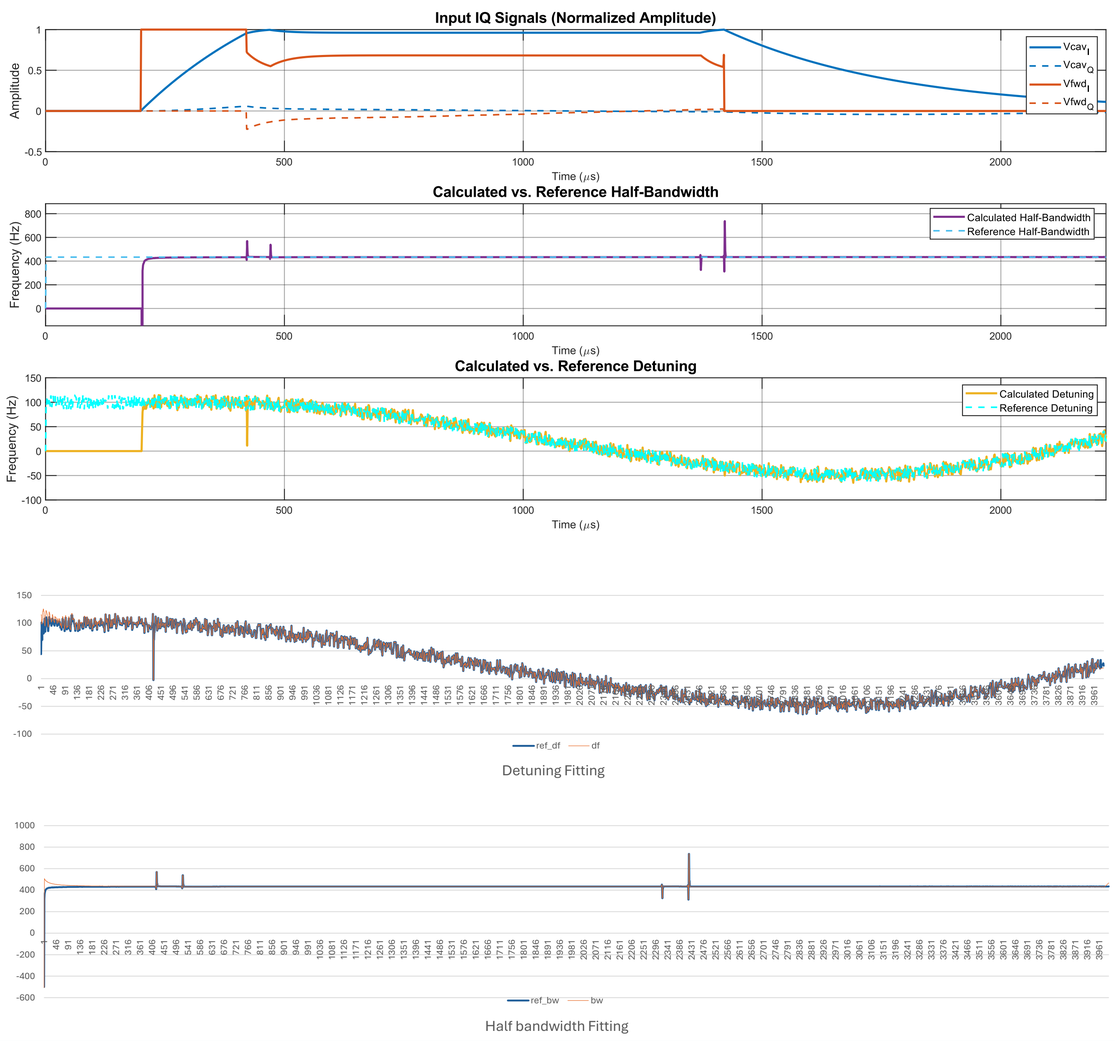

SOFTWARE AND HARDWARE PLATFORM

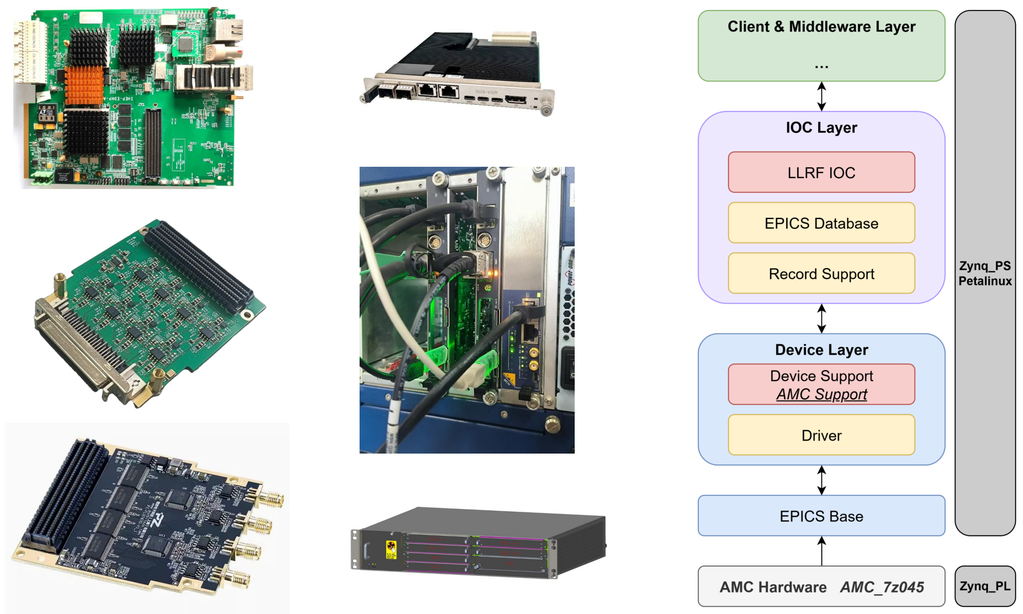

PROGRESS

- **In Progress**
  Firmware integration and testing, calibration module development, upper-layer driver optimization, and EPICS applications are currently underway.
- **Future Plans**
  By June 2026, a horizontal test platform will be established in Huairou, Beijing for the installation and debugging of the LLRF control system.

REFERENCES

[1] Schilcher, T., Schmueser, P., & Gamp, A. (1998). Vector sum control of pulsed accelerating fields in Lorentz force detuned superconducting cavities.
[2] Brandt, A. (2007). Development of a finite state machine for the automated operation of the LLRF control at FLASH (DESY-THESIS--2007-024). Germany
[3] Hoffmann, Matthias (2008). Development of a multichannel RF field detector for the low-level RF control of the free-electron laser at Hamburg (DESY-THESIS--2008-028). Germany
[4] I. Rutkowski, K. Czuba, D. Makowski, A. Mielczarek, H. Schlarb and F. Ludwig, "Vector Modulator Card for MTCA-Based LLRF Control System for Linear Accelerators," in IEEE Transactions on Nuclear Science, vol. 60, no. 5, pp. 3609-3614, Oct. 2013, doi: 10.1109/TNS.2013.2278372.
[5] Gao, J.(2024). CEPC Technical Design Report: Accelerator. Radiat Detect Technol Methods 8, 1–1105. https://doi.org/10.1007/s41605-024-00463-y

*** This work was supported by the National Key Program for ST Research and Development (Grant NO. 2024YFA1610602), Yifang Wang's Science Studio of the Ten Thousand Talents Project, the IHEP Innovation Grant and the National Natural Science Foundation of China (Grant No. 12005240)**

† email address: gann@ihep.ac.cn

中国科学院高能物理研究所
Institute of High Energy Physics, Chinese Academy of Sciences

The 2025 international workshop on the high energy Circular Electron Positron Collider
Track：Accelerator technology Poster ID:28

A14

Superconducting quadrupole magnets in the interaction region of CEPC

Jieru Geng [a, b], Yingshun Zhu [a], Yingzhi Wu [a], Wan Chen [a], Mei Yang [a], Jianxin Zhou [a], Fusan Chen [a], Yuhui Li [a, b]

a Institute of High Energy Physics, Chinese Academy of Sciences, 19B Yuquan Road, Beijing, 100049, China

b University of Chinese Academy of Sciences, 19A Yuquan Road, Beijing, 100049, China

Jieru Geng, IHEP&UCAS
gengjieru@ihep.ac.cn

1 Abstract

This poster presents research on a dual-aperture superconducting quadrupole magnet of CCT type without iron core shielding, which is being designed for the interaction region of the CEPC project. It mainly introduces the direct-winding magnet design scheme and the development of direct-winding technology for fabricating CCT magnets.

2 Introduction

The accelerator of CEPC is now in the engineering design phase, which places more stringent requirements on the design of the superconducting quadrupole magnets in the interaction region. The need to reduce both the weight of the superconducting magnets and the deformation of the cantilevered support has led to the proposal of an ironless magnet solution. As the dual aperture magnets are not shielded by iron yokes, crosstalk will affect the magnetic field quality. For this reason, we propose the ironless dual aperture superconducting quadrupole magnet without correction coils.

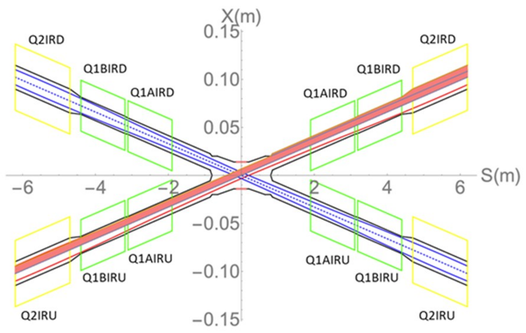

Layout of SCQ magnets in the interaction region.

3 Purpose

The dual-aperture superconducting quadrupole magnet Q1a, with the interaction region closest to the interaction point and the smallest distance between the two apertures in the Higgs mode, is taken as an example. The magnetic field quality problems caused by crosstalk and edge effects between the two apertures of the magnet are solved to meet the EDR requirements for the Q1a magnet.

Item	Value	Unit
Position from the IP	1900	mm
Magnetic field gradient	142.3	T/m
Reference radius	7.46	mm
Magnetic length	1210	mm
Distance between two aperture beam lines at tip	62.71	mm
Integrated field harmonics	≤ 3×10-4	-
Dipole field in aperture	≤ 300	G

Requirements of Q1a magnet.

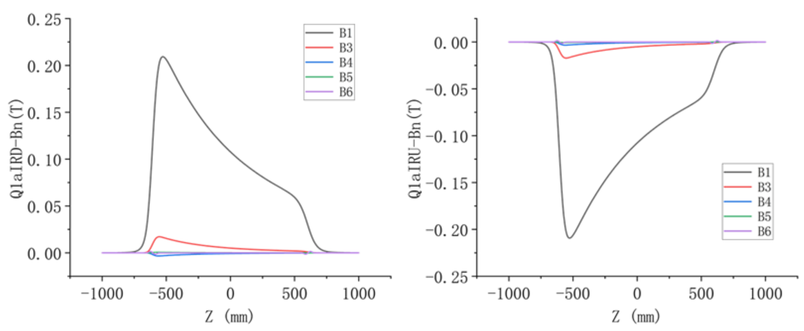

Uncorrected CCT Q1a magnet multipole components.

4 Method

The CCT coil path can be expressed by the equation, and the surface current density is used to derive the corresponding current density distribution of the coil and the magnetic field it generates. Therefore, by modifying the coil path equation, the current density distribution of the coil can be adjusted and new multipole magnetic fields can be added without the corrector coils.

Modified CCT coil path equation:

$$\vec{P}(\theta) = \begin{cases} R\cos\theta \\ R\sin\theta \\ \dfrac{R}{\mathrm{n}\tan(\alpha)}\sin(\mathrm{n}\theta) + \dfrac{\mathrm{w}\theta}{2\pi} + z' \end{cases}, -\pi N \le \theta \le \pi N$$

$$z' = \sum_{n_1}\left(C_m \frac{R\sin(n_1\theta)}{n_1 \tan\alpha}\right) + \sum_{n_2}\left(D_m \frac{R\cos(n_2\theta)}{n_2 \tan\alpha}\right)$$

$$\begin{cases} C_A = (-1)^{n-1} C_{n+m-1}^{n-1} \dfrac{I_B}{I_A}\left(\dfrac{R}{x}\right)^{n+m} \\ C_B = (-1)^{2n+m-1} C_{n+m-1}^{n-1} \dfrac{I_B}{I_A}\left(\dfrac{R}{x}\right)^{n+m} \end{cases}$$

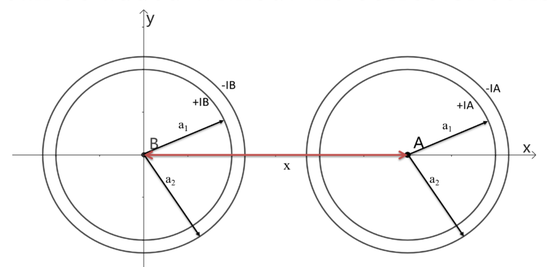

Schematic cross-section of double-aperture magnet.

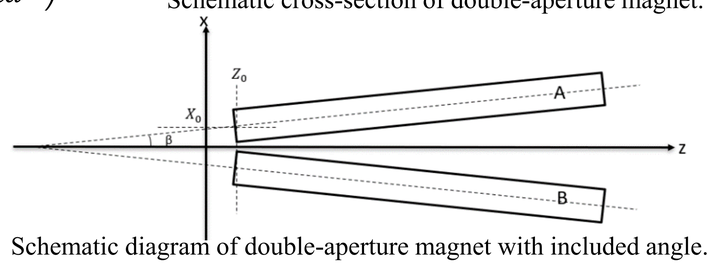

Schematic diagram of double-aperture magnet with included angle.

The beam crossing angle between the two apertures of the superconducting magnet in the CEPC interaction region is 33 mrad, so the distance between the two apertures varies with position.

$$x = 2 \times \left[\left(Z_0 + \frac{R}{2\tan(\alpha)}\sin(2\theta) + \frac{w\theta}{2\pi} + z'\right)\tan\beta + X_0\right]$$

5 Result

$B_n/B_2 \le 3 \times 10^{-4}$

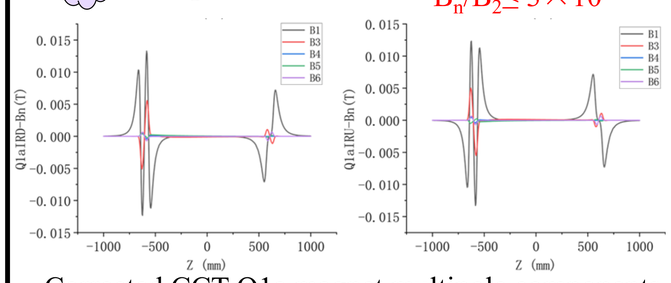

Corrected CCT Q1a magnet multipole components.

The critical aspect of the magnet combination analysis is to determine whether the magnitude of the dipole field amplitude meets the physical requirements after combining Q1a, Q1b, and Q2.

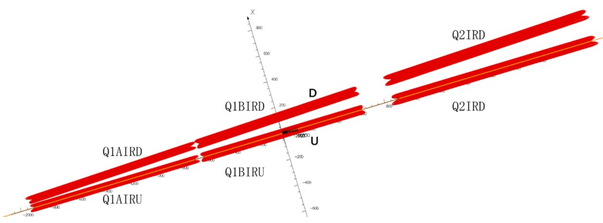

Q1a, Q1b, Q2 magnets 3D model.

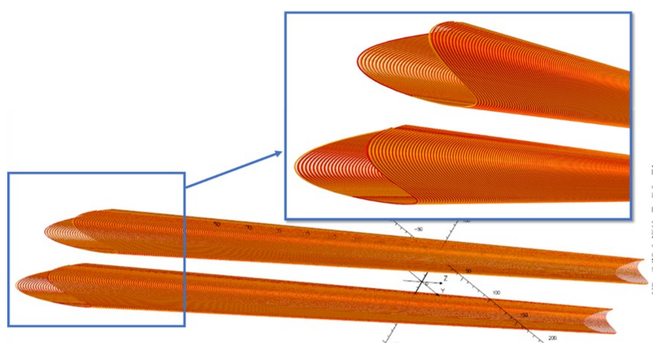

Comparison of single-layer Q1a coil before (red) and after (orange) adjustment.

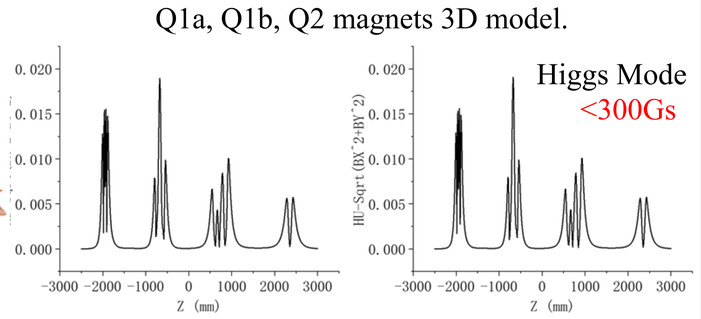

Amplitude of Q1a, Q1b, Q2 dipole field.

6 Direct wind system

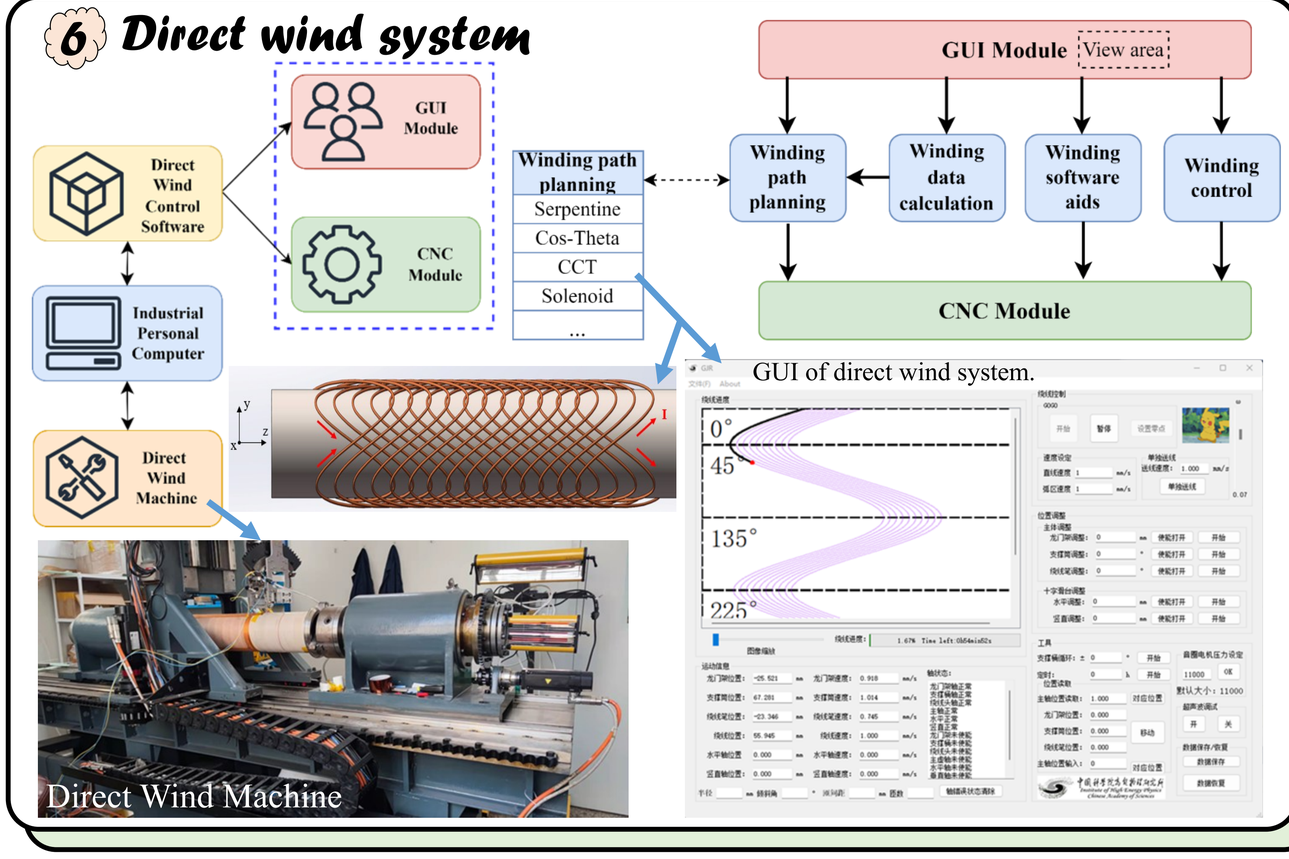

GUI of direct wind system.

Direct Wind Machine

7 Manufacture

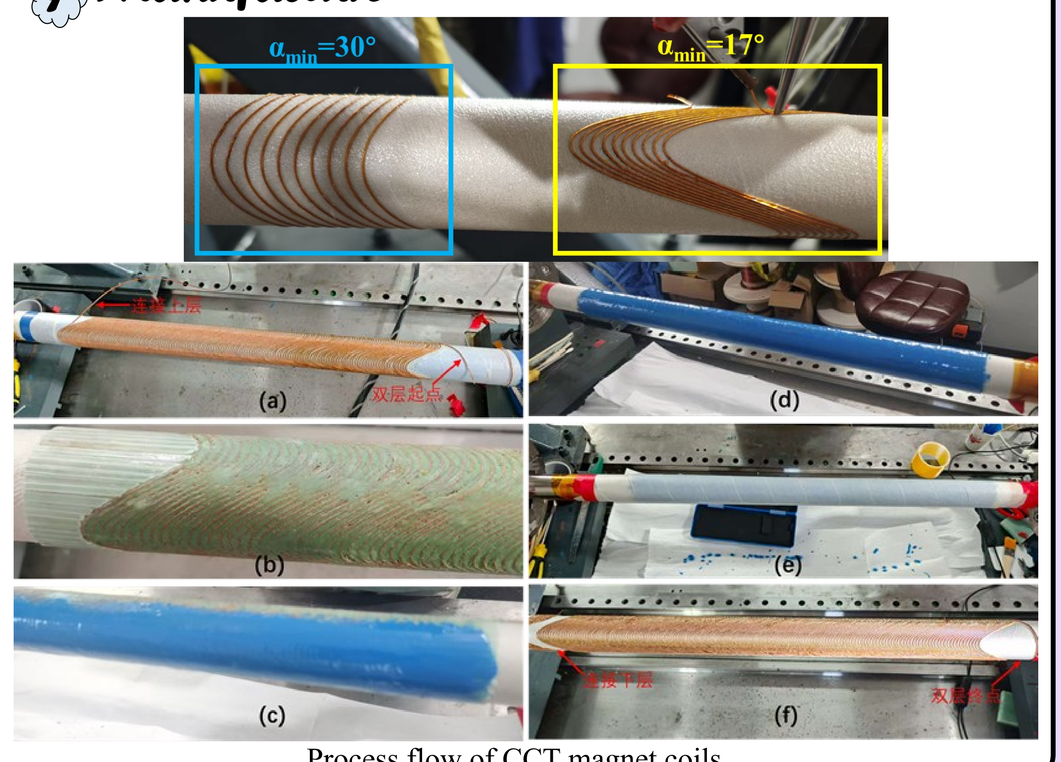

Process flow of CCT magnet coils.

Development of high power energy recovery absorbing load for large scale accelerators

Yang Zhao, Xiang He, Jindong Liu, Fei Li, Wenbin Gao, Ouzheng Xiao, Nan Gan, Yongliang Zeng, Zusheng Zhou*

A-15

Abstract

- In large particle accelerators, the RF power system consumes the most energy. Much unused RF energy is wasted as heat in an absorption load. RF-DC rectification offers a solution to recover this energy, but has historically been impractical due to transistor limitations in handling high power/frequency. Recent GaN transistors have overcome these limitations, reviving interest in this method. This work investigates the feasibility of GaN-based RF rectification and its potential for improving energy efficiency in future colliders like the CEPC.Simulation has achieved 500 MW RF power rectification at S-band using a single module.

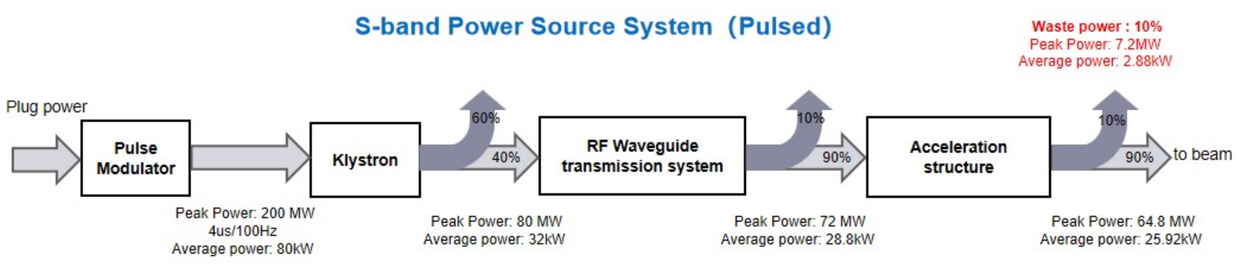

Microwave circuit design

- The energy-recycling load comprises two components: a microwave extraction circuit and an RF rectification circuit. Microwave energy passing through the load is converted into DC power, thereby enabling its secondary utilization.

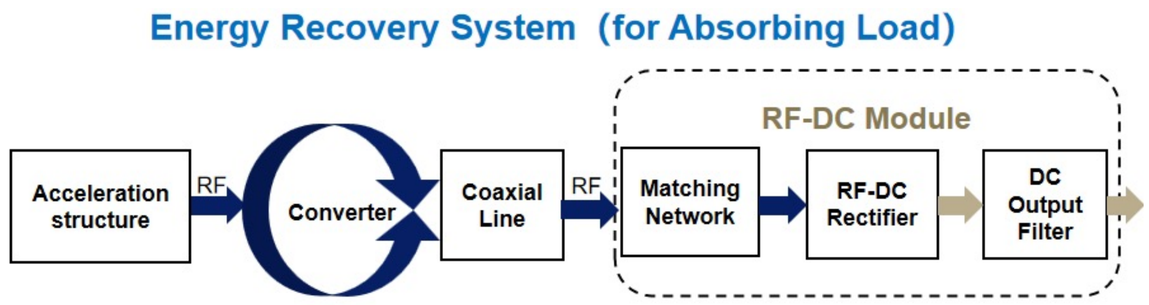

- The microwave extractor design employs the following configuration: An aperture is created on the broad wall of the original microwave absorbing load. A coupling tab extends through this aperture and connects to a coaxial transmission line. By adjusting the insertion depth of the coupling tab, the amount of extracted microwave power can be regulated.

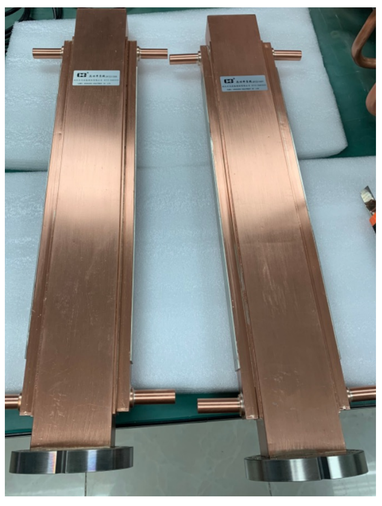

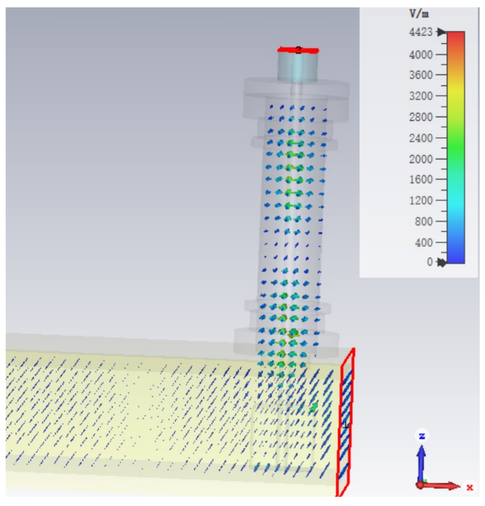

- CST simulation results demonstrate that microwave extraction across a wide frequency range can be achieved while ensuring no reflected waves return to the accelerating structure.

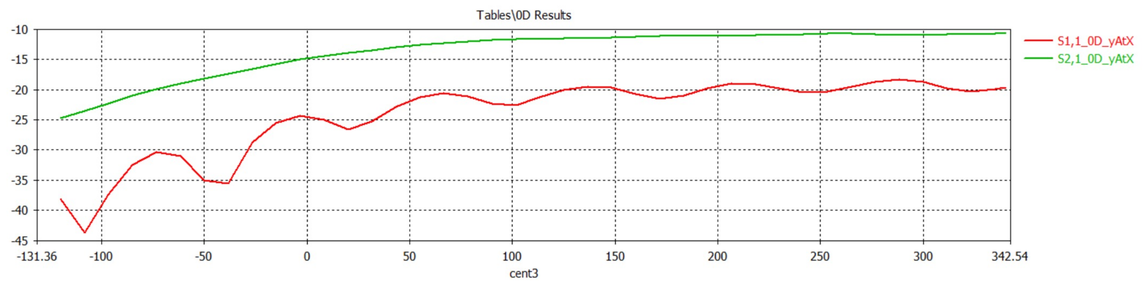

Rectifier circuit design

- The core of the RF rectification circuit design lies in the selection of semiconductor device materials and device types. Both the HEMT based on Gallium Nitride (GaN) material and the LDMOS based on Silicon Carbide (SiC) material possess greater potential for withstanding high-frequency/high-power operation. Therefore, the devices selected for this work are the aforementioned two types.
- Upon determination of the semiconductor devices, the design of the rectification circuit topology needs to be undertaken. Both HEMT and LDMOS are field-effect transistors. The principle of transistor rectification is illustrated in the figure.

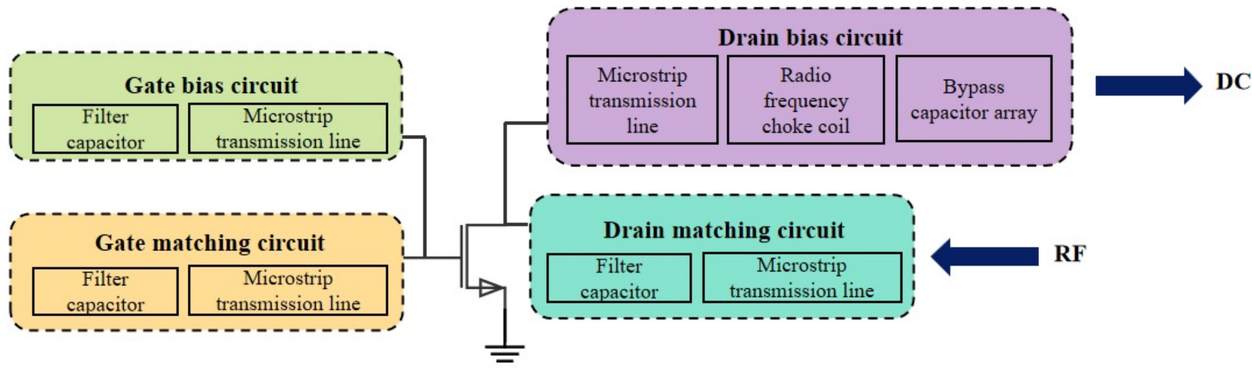

- The circuit structure in the figure below is the schematic diagram of the designed rectification circuit. ADS simulation results demonstrate that when 56 dBm of RF power is fed into the input port of the rectification circuit, 40 dBm of DC power can be obtained at the output port.

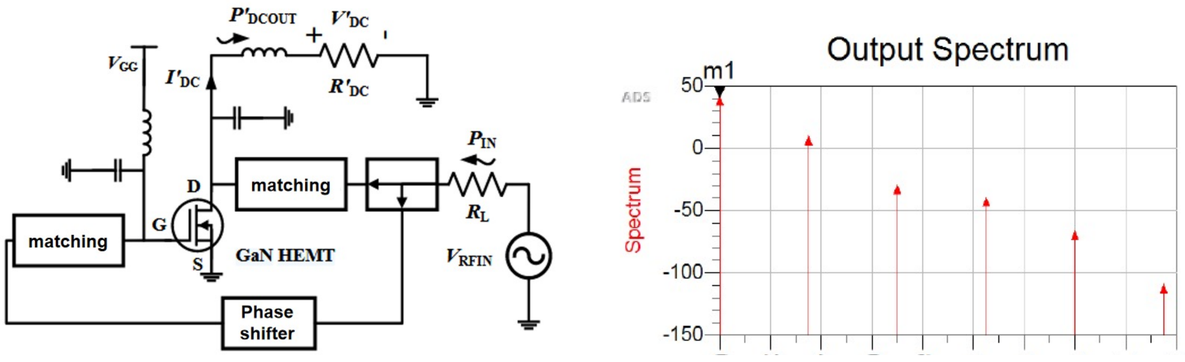

Conclusion

- The results of ADS and CST simulations in this work demonstrate that the unused RF energy in the accelerating structure can be converted into DC power. Although the current conversion efficiency is not high, there remains significant potential for future improvement.